Improving the Efficiency of a Ceria Reduction-oxidation Cycle through the Choice of Operating Conditions and Ceria Morphology

A THESIS SUBMITTED TO THE FACULTY OF THE GRADUATE SCHOOL OF
THE UNIVERSITY OF MINNESOTA
BY

Robert Michael De Smith

IN PARTIAL FULFILLMENT OF THE REQUIREMENTS FOR THE DEGREE OF
MASTER OF SCIENCE

Dr. Jane H. Davidson, Advisor

May, 2014

Acknowledgements

I extend a heartfelt thanks to my family for their support and encouragement throughout my time in graduate school.

I would like to thank my advisor, Dr. Jane H. Davidson, for providing me with the opportunity to participate in such fascinating research in a field of great importance. I am also grateful to many others I have collaborated with in my research: Dr. Luke J. Venstrom, the members of the U of M Solar Energy Lab, Camille Malonzo from the U of M Department of Chemistry, and Will Gibbons from the University of Maryland.

For conversation and companionship throughout the past two years, I thank my Conduction comrades, my Fluids friends, my skydiving accomplices, my roommates Zack Petersen and Michael Gorter, and my office-mate Aayan Banerjee.

The financial support by the U.S. Department of Energy's Advanced Research Projects Agency—Energy (award no. DE-AR0000182) to the University of Minnesota and by the University of Minnesota Initiative for Renewable Energy and the Environment (grants no. RL-0001-09, and RL-0003-11, and RM-0001-12) is gratefully acknowledged.

Dedication

Soli Deo Gloria.

Abstract

Pathways for improving the efficiency of ceria-based thermochemical cycling for solar-driven fuel production are investigated. First, the operating conditions of an isothermal CO_2 splitting cycle are optimized to improve process efficiency. A quasi-equilibrium model is also developed to predict the rates of ceria reduction and oxidation. Finally, a new ceria morphology, wood templated ceria, is examined as a means of improving the heterogeneous oxidation reaction rate by maintaining a high surface area despite exposure to the extreme temperatures required for ceria reduction.

The operating conditions of an isothermal non-stoichiometric ceria redox cycle are optimized. Benchtop experiments at 1500 °C explore the effect of sweep gas and oxidizer (CO_2) flow rates from 50–600 mL min^{-1} g^{-1} for reduction and oxidation periods of ~20 min and ~6 min, respectively. The experimental data are analyzed along with an energy balance on a solar reactor to predict process efficiency and to select the optimum operating conditions (sweep gas and oxidizer flow rates, reduction and oxidation durations). The optimum conditions for isothermal CO production at 1500 °C are a sweep gas flow rate of 150 mL min^{-1} g^{-1}, a CO_2 flow rate of 50 mL min^{-1} g^{-1}, a reduction period of 100 s, and an oxidation period of 155 s. Over 102 cycles, these conditions yielded an average CO production rate of 0.079 μmol s^{-1} g^{-1} and a predicted process efficiency of 4.0%, assuming 3000 suns concentration, 90% heat recovery from the gas streams, and convective losses of 20% of the absorbed solar energy. An analysis of dimensionless scaling parameters shows that the benchtop results can be scaled up to a prototype solar reactor by increasing the gas flow rates in proportion to the ceria mass.

A quasi-equilibrium model is used to predict the rates of isothermal reduction and oxidation as well as of reduction during a temperature ramp. The model is validated for isothermal reduction at 1500 °C with sweep gas flow rates $\leq$ 300 mL min^{-1} g^{-1}, isothermal oxidation at 1500 °C with CO_2 flows of $\leq$ 150 mL min^{-1} g^{-1}, and for reduction during a temperature ramp from 740–1480 °C at 100 °C min^{-1}.

A new ceria morphology for thermochemical fuel production, wood templated ceria, is tested in an infrared imaging furnace at reduction temperatures from 1200–1500 °C and a fixed oxidation temperature of 800 °C to investigate the cycling performance and sintering resistance of the wood templated ceria. The oxidation rate data are analyzed to compare rates obtained for the wood templated ceria to those for a nonporous ceria powder on the basis of ceria non-stoichiometry. The peak CO production rates observed for the wood templated ceria increased with reduction temperature from 1200–1400 °C, reaching 9 mL min^{-1} g^{-1} after reduction at 1400 °C. Reducing at 1500 °C led to substantial sintering of the wood templated structure, decreasing the surface area and lowering the CO production rates significantly. Thus, I recommend the use of the wood templated ceria at a reduction temperature of 1400 °C; at all tested reducing temperatures the reduction and oxidation performance of the wood templated ceria is superior to that of nonporous ceria powder.

Table of Contents

List of Tables

List of Figures

Nomenclature

Roman Letters

a	specific surface area (per unit volume) [m^2 m^{-3}]
C	concentration ratio
c	species concentration [mol m^{-3}]
Da	Damköhler number
$\mathcal{D}_{\mathrm{i,eff}}$	effective diffusion coefficient of species i [m^2 s^{-1}]
F	convective loss factor of reactor
$\bar{G}$	standard relative partial molar Gibbs free energy [J mol^{-1}]
$\bar{H}$	relative partial molar enthalpy [J mol^{-1}]
HHV	higher heating value [J mol^{-1}]
$\bar{h}$	molar enthalpy [J mol^{-1}]
I	direct normal solar irradiance [W m^{-2}]
K	proportionality constant relating reduction and oxidation rates to the rate of change of δ, 2.905×10^{-3} [(mol O_2) (mol ceria) $(\text{mol vac})^{-1}$ $(\text{g ceria})^{-1}$]
K_{eq}	equilibrium constant
L	length of pellet bed [m]
M	metal or molecular weight (of species defined in subscript) [g mol^{-1}]
m	mass [g]
$\dot{n}$	molar production rate or molar flow rate [mol s^{-1}]
Pe_{L}	Peclet number
p	pressure [atm] or partial pressure (subscript defines species) [atm]
q	average rat of thermal energy transfer per unit mass of ceria [W g^{-1}]
R	universal gas constant, 8.314 [J mol^{-1} K^{-1}]
R_{bed}	radius of pellet bed [m]
R'''	reaction rate per unit volume [mol s^{-1} m^{-3}]
$\mathfrak{R}_{\mathrm{ref}}$	reference reaction rate [mol s^{-1} m^{-3}]
r	reaction rate per unit mass ceria [mol s^{-1} g^{-1}]
S_{mix}	mixing enthalpy of gas products [J $cycle^{-1}$ g^{-1}]
$\bar{S}$	relative partial molar entropy [J mol^{-1} K^{-1}]
T	temperature [K]
t	time [s]
U	average gas velocity [m s^{-1}]
$\vec{u}$	local gas velocity [m s^{-1}]
$\dot{V}$	volumetric flow rate, evaluated at 25 °C and 1 bar [mL min^{-1}]
vac	oxygen vacancies in ceria
x	mole fraction (species given in subscript)

Greek Letters

Γ	aspect ratio of pellet bed
Δ	denotes a change in a quantity
$\Delta_r H$	enthalpy change of reaction [J mol^{-1}]
Δt	small step in time [s]
δ	ceria non-stoichiometry (moles of oxygen vacancies per mole of ceria)
ϵ	heat recuperation effectiveness
η	efficiency
ξ	rate of dissociation reaction [mol s^{-1}]
σ	Stefan-Boltzmann constant, 5.670×10^{-8} [W m^{-2} K^{-4}]
τ	duration [s]
ϕ	porosity

Subscripts

amb	ambient
chem	dissociation of CO_2
cycle	cycle
eq	equilibrium
f	fluid
i	gas species
in	evaluated at inlet of pellet bed
loss	solar reactor convection loss
maxima	denotes maximum fuel production rate over range of cycle durations
out	evaluated at the exit of a heat recuperator or the pellet bed
ox	oxidation, oxidizer
R	reactor
red	reduction
ref	reference
reradiation	refers to reradiation from the solar reactor cavity
sg	sweep gas
sink	O_2 sink used to account for ceria oxidation
solar	solar input
th	thermal
tot	total pressure
total	the total molar flow of a gas mixture

Superscripts

′	per unit mass of ceria
″	per unit surface area
$*$	denotes a nondimensional variable
¯	overbar indicates a value averaged over a cycle
ˆ	denotes variable of integration
o	evaluated at inlet conditions

Acronyms/Abbreviations

3DOM	three-dimensionally ordered macroporous
BET	Brunauer−Emmett−Teller
IR	infrared
RLGA	Raman laser gas analyzer
RPC	reticulated porous ceramic
SEM	scanning electron microscope
SSA	specific surface area (per unit mass) [m^2 g^{-1}]
WT	wood templated

1 Introduction

One of the significant challenges facing the world today is the need to produce energy in a manner that does not negatively impact the environment. The vast majority of energy consumption today is based on fossil fuels, but this reliance has some troubling consequences. In addition to the fact that fossil fuels are a finite energy resource[1] in the process of being depleted, burning fossil fuels releases greenhouse gases, which have been linked to global climate change. Increasing global energy demand only exacerbates these issues.

Despite recent efforts in the United States to increase the use of renewable energy, Figure 1.1 shows that only 9.3% of the energy consumed in the country is derived from renewable sources. Of this relatively small amount of renewable energy, only 3.2% (or 0.3% of the total consumption) is solar energy. The sheer magnitude of the earth's solar energy resource (1.7×10^{14} kW of solar power reaches the earth's atmosphere—three orders of magnitude greater than the world's electric consumption [1]) suggests that solar energy could play an important role in meeting the global energy demand in a sustainable manner.

---

[1] Although the energy contained in fossil fuels was ultimately derived from solar energy (a renewable energy source), the natural processes which produce fossil fuels are extremely slow and thus, fossil fuels are not a renewable energy resource on the time scales relevant to human energy demands.

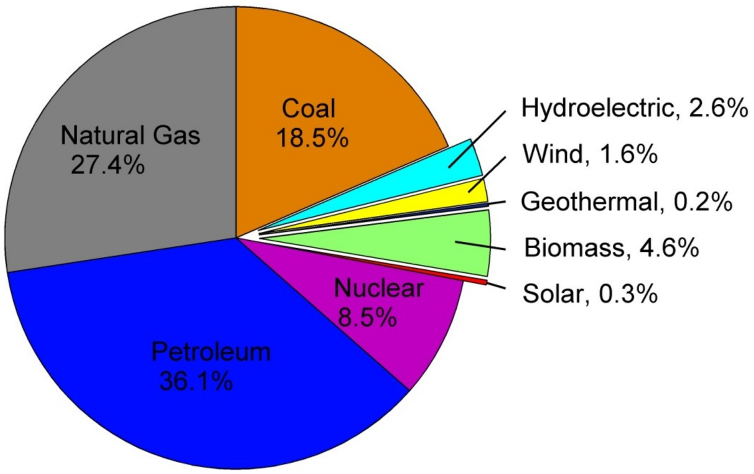

Figure 1.1 2013 energy consumption in the United States by source. Data are from the U.S. Energy Information Administration Monthly Energy Review, March 2014.

One problem standing in the way of large-scale reliance on solar energy is its discontinuous availability, the result of factors both predictable (e.g. night) and unpredictable (e.g. weather). The most straightforward solution to this problem is an efficient method of storing solar energy for later use. One promising method is to use concentrated solar energy to produce chemical fuels such as H_2 and/or CO. A mixture of H_2 and CO, called synthesis gas or syngas, can be either burned directly or converted into conventional liquid hydrocarbon fuels via known chemical processes such as the Fischer-Tropsch process.

One method of producing H_2 and/or CO from feedstocks of H_2O and/or CO_2 involves the reduction-oxidation cycling of a metal oxide. For a metal oxide M_xO_y, the endothermic reduction step is:

$$M_xO_y \rightleftharpoons M_xO_{y-z} + \frac{z}{2}O_2, \tag{1.1}$$

and the exothermic oxidation step is:

$$M_xO_{y-z} + zCO_2 \rightleftharpoons M_xO_y + zCO. \tag{1.2}$$

When the metal oxide undergoes partial reduction (i.e. “z” in equations (1.1) and (1.2) is a non-integer less than y), “z” is replaced with “δ”, the non-stoichiometric coefficient. The net reaction is the splitting of CO_2 into CO and O_2. Analogous equations can be written for H_2 production from H_2O.

This thesis focuses on the redox cycle of equations (1.1) and (1.2) with the metal oxide cerium dioxide (ceria, CeO_2). Chapter 2 introduces the redox cycling of ceria, including two different modes of operation: a temperature swing and an O_2 partial pressure swing. Chapter 3 is a paper (Ref. [2]) which demonstrates the isothermal O_2 pressure-swing operation for CO_2 splitting and presents a method for optimizing the cycle’s gas flow rates and cycling periods to maximize process efficiency. A model for predicting the rates of reduction and oxidation is developed and validated in Chapter 4. Chapter 5 reviews previous work with ceria morphologies and presents the experimental testing of wood templated ceria[2] (a morphology not previously studied for solar-driven ceria redox cycling) and a nonporous ceria powder. The reduction and oxidation performance of the wood templated ceria is studied over a range of reduction temperatures (1200–1500 °C), and the performance of the wood templated ceria is compared with that of the nonporous ceria using a novel method of comparing oxidation rate data as a function of ceria non-stoichiometry.

---

[2] Wood templated ceria is synthesized by Camille Malonzo, advised by Dr. Andreas Stein (University of Minnesota, Department of Chemistry).

2 Solar Fuel Production with Non-stoichiometric Ceria

2.1 Introduction to Redox Cycling

The most basic way to split H_2O or CO_2 is via direct thermolysis. However, the required temperatures for this reaction are 2200 °C or greater [3,4]—substantially higher than the theoretical optimum solar reactor temperatures of 800–1500 °C reported by Ref. [3] for typical tower or dish concentrating systems. In addition, direct thermolysis of H_2O or CO_2 requires the separation of reaction products at very high temperatures to avoid recombination. An efficient process to accomplish this high temperature separation has not yet been identified [3–5]. Two-step processes for splitting H_2O or CO_2 involving metal oxides lower the required temperatures and circumvent the gas separation problem by releasing O_2 and H_2/CO in separate steps.

Several metal oxides have been studied for redox cycling; promising candidates include zinc oxide, iron-based oxides (ferrites), and ceria. Zinc oxide (ZnO) undergoes complete reduction (i.e. “z” in equations (1.1) and (1.2) is an integer less than or equal to y), allowing for relatively high fuel production per mole of ZnO, but its volatility requires energy-intensive rapid quenching to prevent recombination of reduction products [3,6]. Other metal oxides, such as the ferrites and ceria, can undergo partial reduction (i.e. “z” in equations (1.1) and (1.2) becomes “δ”, the non-stoichiometric coefficient, which is a non-integer less than y) while remaining nonvolatile if the metal oxides are reduced in a low-oxygen environment. However, ferrites sinter severely, losing surface area and slowing reaction rates. This sintering can be alleviated by supporting the ferrite with zirconia (ZrO_2) [7,8], although this approach incurs an energy penalty as the largely inert ZrO_2 must be heated and cooled along with the reactive ferrite.

Ceria offers potential for efficient production of H_2 and/or CO via solar-driven non-stoichiometric redox cycling. At temperatures feasible for solar reactors (800–1500 °C [3]), ceria can attain an appreciable extent of reduction (e.g. $\delta = 0.06$ at 1500 °C with $p_{O_2} = 10^{-5}$ atm) [9]. Furthermore, ceria possesses a melting temperature of ~2500 °C—far above the anticipated reactor temperatures, so volatilization is avoided, and ceria can undergo significant reduction ($\delta = 0.25$ above 1000 °C) without changing its cubic fluorite crystal structure [10]. Long-term stability of ceria redox cycling has been demonstrated [2,10–12] without requiring an inert support. Because of these advantages, ceria is the metal oxide studied in this thesis.

2.2 Thermodynamics of Ceria

For the non-stoichiometric redox cycling of ceria, equations (1.1) and (1.2) are rewritten, allowing for the possibility that the ceria begins at a nonzero non-stoichiometry (δ_{ox}):

$$CeO_{2-\delta_{\mathrm{ox}}} \rightleftharpoons CeO_{2-\delta_{\mathrm{rd}}} + \frac{(\delta_{\mathrm{rd}} - \delta_{\mathrm{ox}})}{2} O_2 \tag{2.1}$$

for reduction and

$$CeO_{2-\delta_{\mathrm{rd}}} + (\delta_{\mathrm{rd}} - \delta_{\mathrm{ox}})CO_2 \rightleftharpoons CeO_{2-\delta_{\mathrm{ox}}} + (\delta_{\mathrm{rd}} - \delta_{\mathrm{ox}})CO \tag{2.2}$$

for oxidation. Over a cycle, the fuel production is proportional to the swing in non-stoichiometry that is achieved between its reduced and oxidized state, $(\delta_{\mathrm{rd}} - \delta_{\mathrm{ox}})$.

The equilibrium non-stoichiometry of ceria is a function of both temperature (T) and the oxygen partial pressure (p_{O_2}) surrounding the ceria. This functional dependence has been measured experimentally via thermogravimetric measurements, and is reported by Panlener *et al.* [9] as the relative partial molar enthalpy ($\Delta\bar{H}_{O_2}$) and entropy ($\Delta\bar{S}_{O_2}$), which are found to depend on δ but not on temperature[3]. These thermodynamic parameters are defined using the reaction

$$\lim_{z\to 0}\left[O_2 + \frac{2}{z}CeO_{2-\delta} \rightleftharpoons \frac{2}{z}CeO_{2-\delta+z}\right]. \tag{2.3}$$

Evaluating reaction (2.3) at a reference pressure (p_{ref}) of 1 atm and assuming ideal gas behavior, the equilibrium condition is expressed as

$$\Delta\bar{G}_{O_2} = -RT\ln\left(K_{\mathrm{eq}}\right) = RT\ln\left(\frac{p_{O_2}}{p_{\mathrm{ref}}}\right), \tag{2.4}$$

where $\Delta\bar{G}_{O_2}$ is the standard relative partial molar Gibbs free energy, defined in terms of the reported thermodynamic properties as

$$\Delta\bar{G}_{O_2} = \Delta\bar{H}_{O_2} - T\Delta\bar{S}_{O_2}. \tag{2.5}$$

Combining equations (2.4) and (2.5) yields

$$RT\ln\left(\frac{p_{O_2}}{p_{\mathrm{ref}}}\right) = \Delta\bar{H}_{O_2} - T\Delta\bar{S}_{O_2}, \tag{2.6}$$

---

[3] This observation allows the thermodynamic behavior of ceria to be ascertained at temperatures higher than those experimentally tested. This was used to extend the scope of Figure 2.1 beyond the 1500 °C maximum temperature of the data in Ref. [9].

which, paired with experimental data for $\Delta\overline{H}_{O_2}$ and $\Delta\bar{S}_{O_2}$ as a function of δ, can be used to calculate the equilibrium non-stoichiometry of ceria as a function of temperature and oxygen partial pressure.

This procedure was employed along with the experimental data from Ref. [9] to create Figure 2.1, which illustrates the dependence of δ on T and p_{O_2}. The isotherms in Figure 2.1 (gray lines) show that large departures from stoichiometry are favored at high temperatures and low oxygen partial pressures; the non-stoichiometry during reduction, δ_{rd}, is limited by the maximum operating temperature of a solar reactor and the minimum p_{O_2} that can be achieved (e.g. with an inert sweep gas with very low O_2 content). The black solid and dashed lines in Figure 2.1 represent the equilibrium states of ceria under a range of gas atmospheres feasible for the oxidation step (CO_2 and H_2O, each at 100% and 20% in an inert carrier), and thus show the minimum non-stoichiometries for these oxidation conditions (i.e. minimum δ_{ox}). Figure 2.1 suggests two basic strategies of achieving a change in δ (and thus producing fuel): a temperature swing [10,11,13–19] or an isothermal oxygen partial pressure swing [20,21]. These two strategies are discussed in the following section.

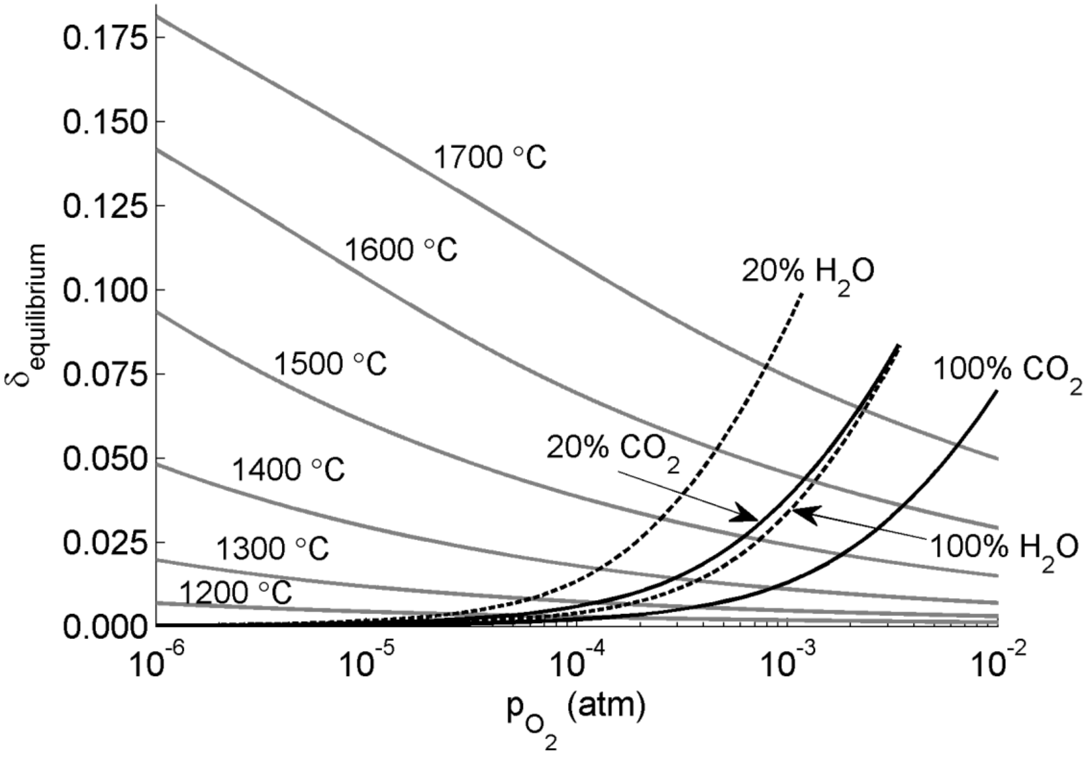

Figure 2.1 State diagram for undoped ceria with isothermal plots of the equilibrium state for a range of oxygen partial pressures. The diagram was constructed using thermodynamic data from Ref. [9]. The equilibrium states for oxidation with 20% and 100% CO_2 (solid black lines) and 20% and 100% H_2O (dashed black lines) at a total pressure of 1 atm are also plotted as a function of temperature. Where these lines cross the isothermal lines sets a bound on the extent to which the reduced ceria can be re-oxidized.

2.3 Temperature-swing vs. O_2 Partial Pressure-swing Operation[4]

Most prior work has focused on the temperature-swing approach to cycling ceria because large changes in non-stoichiometry are favored when ceria is reduced at high

---

[4] Section 2.3 appears in Ref. [2], and is used with permission (see note on p. 13).

temperature and low oxygen partial pressure and oxidized at lower temperature. For example, chemical thermodynamics predicts that a swing from reduction at 1500 °C and p_{O_2} = 10^{-2} atm to oxidation at 800 °C yields $\Delta\delta$ = 0.015, irrespective of the oxidant (H_2O or CO_2) or, within reasonable bounds, its concentration. The temperature-swing cycle has been implemented in a prototype solar reactor in which an inert sweep gas was used to achieve low oxygen partial pressure during reduction [15–17]. The average solar-to-chemical energy efficiency, defined as the energy of the produced fuel divided by the required solar input, was 1.7% for CO production in a batch process after the duration of reduction was selected for maximum efficiency [17]. Thermodynamic analysis of the process shows that higher efficiencies are possible with recuperation of the sensible heat of the sweep and oxidizing gas streams as well as of the sensible heat of the solid ceria [18]. Although approaches to achieve continuous solid phase heat recuperation have been proposed [19,22,23], they have either had limited success or they have not been implemented in a working reactor. Recovery of the sensible heat of the gases is also a challenge due to the material constraints for the heat exchanger at the reduction temperatures required for appreciable fuel production. Less gas phase heat recuperation is required if the amount of sweep and oxidizing gas can be reduced without also decreasing the change in non-stoichiometry achieved in the cycle.

The isothermal pressure-swing cycle eliminates the need for solid phase heat recuperation [20,21,24] at the penalty of increased need for gas phase heat recovery. This penalty arises because the oxidant must be heated to a higher temperature than in the case of the temperature-swing cycle and because a greater swing in gas composition is required to produce a given change in non-stoichiometry than in the case of the temperature-swing cycle—that is, a lower oxygen partial pressure is required in the reduction step and/or a higher concentration of the oxidant is required in the oxidation step (Fig. 2.1). For example, to achieve the same change in non-stoichiometry in the isothermal cycle at 1500 °C when CO is produced from 100% CO_2 as that of the temperature-swing cycle from 1500 °C and $p_{O_2} = 10^{-2}$ atm to 800 °C, the oxygen partial pressure during reduction must be $p_{O_2} = 1.4\times10^{-4}$ atm. If the CO is produced from 20% CO_2 instead of 100% CO_2, a further reduction in the oxygen partial pressure during reduction to $p_{O_2} = 6.9\times10^{-5}$ atm is required. If H_2 is produced from 20% H_2O, the oxygen partial pressure required must be even further reduced to $p_{O_2} = 3.7\times10^{-5}$ atm (Fig. 2.1) because H_2O has a lower oxygen activity than CO_2 at temperatures above 810 °C [5]. To maintain low oxygen partial pressure during reduction, a sweep gas and/or operation below atmospheric pressure is required. Operation at less than atmospheric pressure has yet to be demonstrated in the literature. Without 100% gas-phase sensible heat recovery (an idealization), the challenge for efficient fuel production is to reduce the amount of sweep gas and CO_2 used in the cycle while maintaining a rapid rate of fuel production. Rate data are thus required over a range of gas flow rates and cycling periods (the durations of reduction and oxidation) to select the operating conditions that maximize efficiency.

The viability of isothermal redox cycling of ceria for hydrogen production has been demonstrated in an initial, proof of concept experimental study [21]. Though the

---

[5] At 810 °C, the changes in Gibbs free energy of the dissociation of CO_2 and H_2O are equal.

range of conditions considered was insufficient for optimization of the gas flow rates and cycling periods, it was possible to infer from the data that an average rate of H_2 production comparable to that of the temperature-swing cycle would be achievable when the temperature-swing cycle is subject to appropriate finite heating and cooling rates [21]. The present study demonstrates that isothermal redox cycling is also capable of producing CO at rates comparable to the temperature-swing cycle.

2.4 Challenges of Ceria Redox Cycling

Several obstacles remain to the implementation of solar-driven ceria redox cycling. Two avenues of analyzing the ceria cycle have been commonly used in the past; each has strengths and weaknesses. The first method predicts the maximum possible process efficiency by modeling ceria's behavior with equilibrium thermodynamics and accounting for the energy requirements of a redox cycle (e.g. heating gas flows, reradiation losses, convection losses, etc.) [10,18–21,25,26]. The second method determines redox cycle performance experimentally, either on a benchtop scale [10,11,13,14,21] or a prototype reactor scale [15–17]. While the first method is useful for understanding the ceria redox cycle and identifying key parameters for efficient operation, the idealizations that studies using this method rely on often lead to predicted efficiencies an order of magnitude higher than what has, to date, been experimentally demonstrated[6]. While the experimental studies provide real (rather than theoretical) efficiencies, they often use cycling conditions such as gas flow rates and cycling periods

---

[6] See Section 4.4 for a discussion of the common yet unrealistic assumption of achieving equilibrium during reduction with a high-purity sweep gas.

that are chosen somewhat arbitrarily; little effort has been spent on identifying cycling conditions which lead to the maximum efficiency, although Furler *et al.* [17] identified optimum reduction durations to maximize the efficiency of a prototype solar reactor operating a ceria temperature swing cycle in batch mode. Chapter 3 of this thesis addresses some of the weaknesses of each method by using experimental data (rather than equilibrium thermodynamics) as the basis for predicting realistically attainable efficiencies and by developing a method for optimizing the cycling conditions for isothermal operation of a ceria thermochemical cycle.

Identifying ceria morphologies suitable for high-temperature cycling is another challenge. Since the reduction and oxidation of ceria are heterogeneous reactions, morphologies with high surface areas are desired. The difficulty lies in finding a microstructure capable of retaining a high surface area when exposed to the high temperatures necessary for reduction, which can cause significant sintering of high surface area morphologies. Although several morphologies have been reported in the literature, including porous monoliths [10,15,21], structured powders [11,13,14], felt [16], electrospun fibers [12], and reticulated porous ceramics (RPC) [17,27], the wide range of operating conditions under which they have been tested make the results difficult to compare. Chapter 5 of this thesis contributes to this area of research by exploring the cycling performance of a new ceria morphology (wood templated ceria) and demonstrating a method for comparing oxidation rates as functions of ceria non-stoichiometry, allowing straightforward comparison of samples which began oxidation at different non-stoichiometries.

3 Efficient Splitting of CO_2 in an Isothermal Pressure-swing Redox Cycle based on Ceria[7]

This chapter presents the first measurements of CO production rates from CO_2 splitting in an isothermal ceria redox cycle. Data obtained for a wide range of flow rates of inert sweep gas and CO_2 are interpreted to determine optimal flow rates and cycling periods and to provide a realistic assessment of the process efficiency. Prior theoretical estimates of efficiency assume optimistically low gas flow rates and thermodynamic fuel production [20]. To reduce the number of experiments required to identify the gas flow rates and cycling periods that lead to the most efficient production of CO, a technique is developed to analyze reaction rate data collected in cycles of extended duration to predict fuel production for shorter cycles. An energy balance on a solar reactor is used to evaluate the required solar input so that cycle efficiency can be calculated. The approach is also applicable to the production H_2 or the simultaneous production of CO and H_2. Similitude allows extrapolation of the operating conditions identified in a bench top reactor for efficient CO production to operation of prototype or industrial scale reactors.

---

[7] Chapter 3 is reproduced with permission from:
Venstrom, L. J., De Smith, R. M., Hao, Y., Haile, S. M., and Davidson, J. H., 2014, "Efficient Splitting of CO_2 *in an Isothermal Redox Cycle Based on Ceria," Energy & Fuels,* ***28****(4), pp. 2732–2742.*

This work was completed with the assistance of a number of collaborators. I collected and analyzed experimental data, developed and carried out the procedures for optimizing gas flow rates and cycling periods, and implemented the energy balance to predict cycle efficiency. Luke J. Venstrom assisted in the collection and interpretation of the experimental data, developed the scaling procedure, and was instrumental in writing the text. Jane H. Davidson provided editorial contributions; Yong Hao and Sossina Haile provided the ceria used in the experiments.

3.1 Approach

3.1.1 Reactive Substrate Configuration

A bed of porous pellets was the configuration selected for the experimental testing of ceria. Porous ceria pellets were prepared by cutting a porous ceria monolith (synthesis procedure is described in Ref. [2]) into 3–5 mm pieces. The microstructure of the pellets, shown in Figure 3.1, has pores and solid features on the order of a micrometer and a porosity of ~65% (for a single pellet). The small feature sizes, along with the very high chemical diffusivity of oxygen through ceria, indicate that oxygen diffusion through the ceria is unlikely to be rate-limiting [2]; this conclusion is supported by experimental observations for isothermal H_2 production [21].

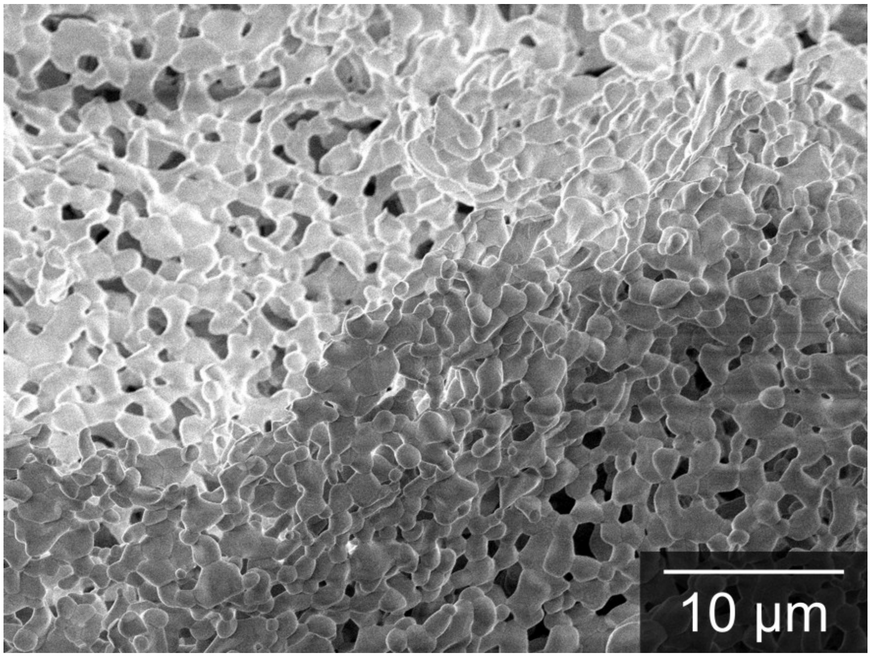

Figure 3.1 SEM image of the porous pellet surface revealing its microstructure to be a randomly-oriented network of pores with diameters on the order of micrometers.

Refs. [2] and [28] describe the benefits of the bed of porous ceria pellets. Gases flow through the voids in the bed rather than the pores of pellets, so the pressure drop across the bed is low compared to a porous monolith or a packed bed of powder. The dimensionless Wagner modulus [29,30] for the pellets is found to be less than 0.15, indicating that diffusion of reactants or products through the pores of the pellets does not limit the reactions. Heat transfer rates within the bed and within the pellets themselves are found to be favorable, and the specific surface area (an important quantity for heterogeneous reactions) is relatively high, $\sim 2\times10^5$ m^{-1}.

3.1.2 Measurement of Reduction and Oxidation Rates

Experiments to explore the impact of inert sweep gas and CO_2 flow rates on the rates of O_2 and CO production were conducted at 1500 °C. Figure 3.2 is a sketch of the experimental apparatus. The porous pellets (1.0245 grams) were packed in a high-density, high-purity 13 mm o.d., 9.5 mm i.d. alumina tube over a length of 10 mm into a bed with a void fraction of ~45%. The alumina tube containing the pellets was heated in an IR imaging furnace. No reaction was observed between the alumina tube and the ceria. Two alumina-sheathed Pt/Pt-Rh thermocouple probes with exposed junctions were placed in contact with the upstream and downstream faces of the packed bed to monitor temperature. Sweep gas (10.6±0.1 ppm O_2 in N_2) and CO_2 (99.99% pure) were delivered using high-accuracy (±1% of reading) mass flow controllers. Rapid switching (< 50 ms) of the sweep gas and CO_2 streams between reduction and oxidation was achieved with pneumatic valves. Flow rates were varied between 50 and 600 mL min^{-1}. Flow rates lower than 50 mL min^{-1} led to O_2 and CO concentrations in the product stream below the detection limit of the Raman laser gas analyzer (detectable limit of 0.01 mol% and accuracy of ±0.02 mol%), and flow rates higher than 600 mL min^{-1} led to convective cooling of the porous pellets below the desired 1500 °C operating point. The transient global rates of O_2 and CO production were calculated by

$$\dot{n}_{\mathrm{i}}' = \frac{x_{\mathrm{i}}\dot{n}_{\mathrm{total}}}{m_{\mathrm{CeO_2}}}, \tag{3.1}$$

where $\dot{n}_{\mathrm{i}}'$ is the rate of O_2 or CO production per unit mass of CeO_2.

Prior to reduction, the porous ceria pellets were initialized to a non-stoichiometry of 0.021 via equilibration in CO_2 at 1500 °C. To initiate reduction, the CO_2 flow was rapidly replaced with the flow of sweep gas, and the sweep gas flow was sustained for 20 min. This period of time was selected despite not reaching thermodynamic equilibrium in recognition that longer cycle durations require excessive use of sweep gas while yielding substantially lower average rates of fuel production. Oxidation was initiated by switching to a flow of CO_2 and continued until the ceria returned to its initial equilibrium state. Equilibration required less than 6 min.

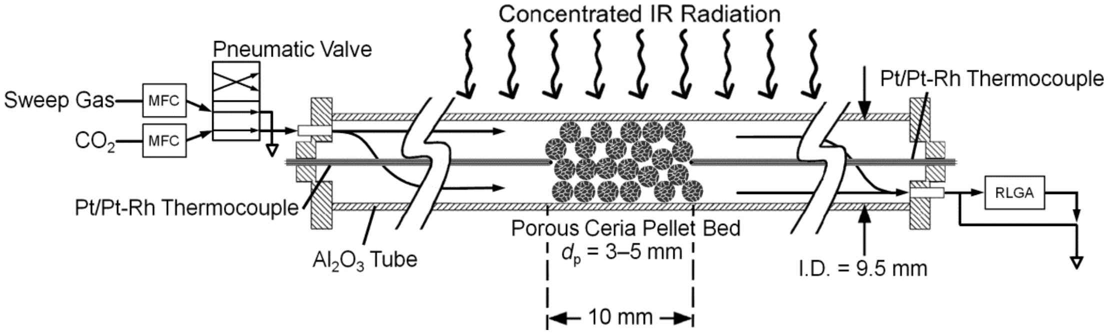

Figure 3.2 Sketch (not to scale) of the isothermal pressure-swing reactor featuring a packed bed of mm-scale porous ceria pellets.

3.1.3 Optimization of Cycling

The reduction and oxidation rate data, collected over 20 min and 6 min, respectively, were analyzed to predict fuel production as a function of both gas flow rate and cycle duration. This approach allows one to optimize the cycle for efficient fuel production without independently varying experimental reduction and oxidation times, a prohibitively time-consuming task due to the number of possibilities.

The average molar rate of fuel production per unit mass of ceria for steady cycling is

$$\overline{\dot{n}_{\mathrm{CO}}'} = \frac{\Delta\delta}{\mathrm{M}_{\mathrm{CeO_2}}\tau_{\mathrm{cycle}}} = \frac{\delta_{\mathrm{rd}} - \delta_{\mathrm{ox}}}{\mathrm{M}_{\mathrm{CeO_2}}\,(\tau_{\mathrm{rd}} + \tau_{\mathrm{ox}})}, \tag{3.2}$$

where τ_{cycle} is the duration of the cycle—the sum of the reduction period, τ_{rd}, and the oxidation period, τ_{ox}. The time required to achieve a given change in the non-stoichiometry is obtained by integrating the transient O_2 and CO production during reduction and oxidation. This approach requires a reaction substrate that is not limited by solid-state oxygen diffusion, for which the rate of reaction is independent of the initial state of ceria. As noted earlier, porous substrates, like the porous pellet packed bed of the present study, satisfy this condition. Referenced to the ceria non-stoichiometry when it is equilibrated with the oxidant (δ_{eq}, corresponds to the intersection of the 1500 °C isotherm line and the line for equilibrium with 100% CO_2 in Fig. 2.1), the change in the spatial average non-stoichiometry over the duration t_{rd} for reduction is

$$\left(\delta - \delta_{\mathrm{eq}}\right)_{\mathrm{rd}} = M_{\mathrm{CeO_2}} \int_{0}^{t_{\mathrm{rd}}} 2\dot{n}_{\mathrm{O_2}}' dt\,. \tag{3.3}$$

For oxidation, the change in the average non-stoichiometry over the duration t_{ox} is

$$\left(\delta - \delta_{\mathrm{eq}}\right)_{\mathrm{ox}} = M_{\mathrm{CeO_2}} \int_{t_{\mathrm{eq}}-t_{\mathrm{ox}}}^{t_{\mathrm{eq}}} \dot{n}_{\mathrm{CO}}' dt\,, \tag{3.4}$$

where t_{eq} is the time at which the ceria reaches equilibrium with the oxidant flow.

The non-stoichiometry-time relations provide for all possible combinations of δ_{rd} and δ_{ox} the corresponding reduction and oxidation periods and, via equation (3.2), the average rate of fuel production for each combination of sweep gas and CO_2 flow rates. As an illustration, Figure 3.3 shows the δ-time relations for sweep gas and CO_2 flow rates of 581 and 297 mL min^{-1} g^{-1}, respectively. Consider the case where ceria is cycled using these gas flow rates, but with shorter cycle times such that the ceria cycles between $\delta_{\mathrm{rd}} = \delta_{\mathrm{eq}} + 0.015$ and $\delta_{\mathrm{ox}} = \delta_{\mathrm{eq}} + 0.005$. In this case, τ_{rd} = 9.5 min and τ_{ox} = 0.9 min with an average fuel production rate of 0.093 μmol s^{-1} g^{-1}, as indicated in Figure 3.3.

This procedure is repeated for thousands of combinations of δ_{rd} and δ_{ox} to map the reduction and oxidation periods to the corresponding average rate of fuel production. Figure 3.4 shows the mapping on a surface plot for the same gas flow rates represented in Figure 3.3. The saddle in the CO production rate surface (emphasized with a dark, solid line) reveals the reduction and oxidation periods that lead to the most rapid rate of CO production for a given selection of the cycle duration. On the inset of Figure 3.4, the rates of CO production achieved for the reduction and oxidation periods on the saddle are plotted versus cycle duration from 20 s to 200 s. The maximum average rate of CO production is 0.225 μmol s^{-1} g^{-1}, achieved as the cycle duration approaches zero. This trend holds for all combinations of sweep gas and CO_2 flow rates.

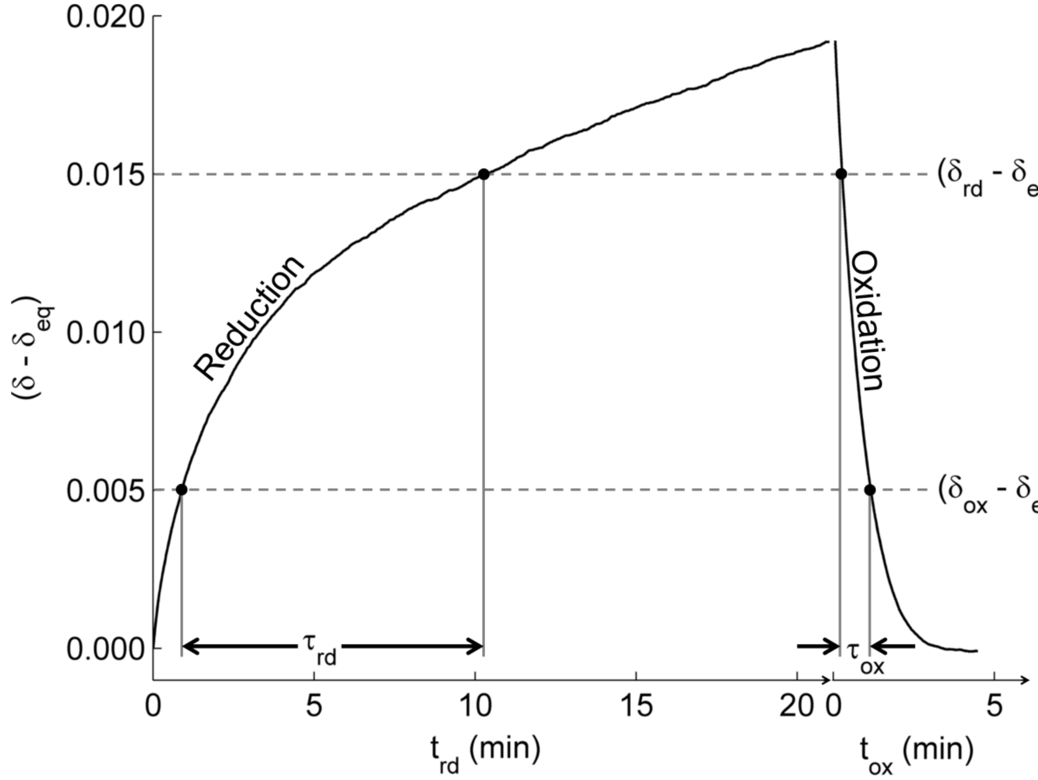

Figure 3.3 Non-stoichiometry-time relations for a sweep gas flow rate of 581 mL min^{-1} g^{-1} and a CO_2 flow rate of 297 mL min^{-1} g^{-1}. The reduction and oxidation periods (τ_{rd} and τ_{ox}) corresponding to cycling between $\delta_{rd} = \delta_{eq}+0.015$ and $\delta_{ox} = \delta_{eq}+0.005$ are indicated by the solid vertical lines. $\delta_{eq} = 0.021$.

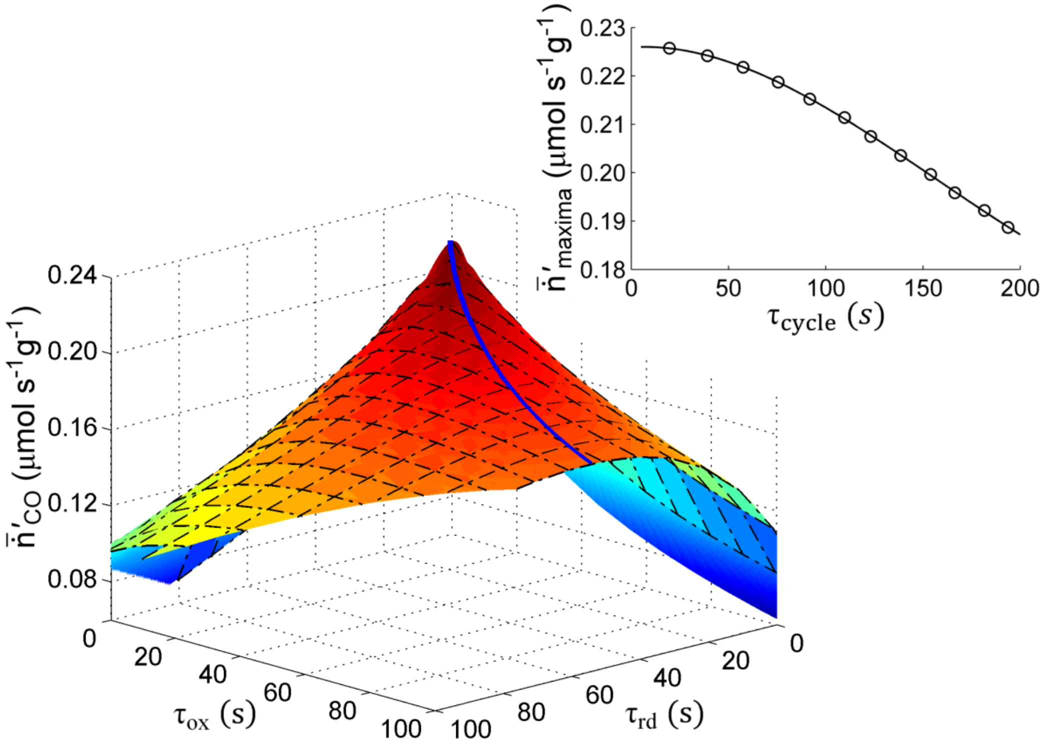

Figure 3.4 Mapping of the reduction (τ_{rd}) and oxidation (τ_{ox}) periods to the average rate of CO production using the data of Figure 3.3. The locus of maximum average rates of CO production, shown as a function of the cycling period ($\tau_{cycle} = \tau_{rd} + \tau_{ox}$) on the inset, is emphasized with a solid line.

Flow rates and cycling periods are then selected to maximize efficiency based on reasonable assumptions for operation of the cycle in a solar reactor in which the porous pellets are in alumina tubes within a cavity receiver (such as the reactor presented in Ref. [28]). The reducing and oxidizing atmospheres are alternated by flowing the appropriate gases through the tubes. The projected thermal efficiency is expressed on a per unit mass basis,

$$\eta_{\text{th}} = \frac{\overline{\dot{n}_{\text{CO}}^{'}} \times \text{HHV}_{\text{CO}}}{q_{\text{solar}}}, \tag{3.5}$$

where the average rate of fuel production and the required solar input are functions of the operating conditions of the cycle (gas flow rate and cycling periods). The denominator includes the solar power required for heating gases and to compensate for thermal losses but neglects the thermal equivalent of parasitic processes, including, for example, the pumping power or the power required to separate the O_2 and CO from the sweep gas and CO_2 flows. These parasitic requirements are small relative to the terms included in the energy balance on the solar reactor (equation (3.6)) but require attention in practice. For example, the power required to separate gases can be minimized by recycling the sweep gas and CO_2 flows in the process [20]. The fuel production rate is obtained from experimental data using the analysis detailed above. The incorporation of reaction rate data into the projected efficiency represents a substantial departure from prior thermodynamic studies [18,20,21,25] and has the advantage of providing realistic, rather than theoretical, estimates of efficiency. The solar input that would be required to drive the cycle is determined from an energy balance on a hypothetical solar receiver/reactor,

$$q_{\text{solar}} = q_{\text{reradiation}} + q_{\text{loss}} + q_{\text{sg}} + q_{\text{ox}} + q_{\text{chem}}. \tag{3.6}$$

Each flow of energy is evaluated per unit mass of ceria and is averaged over a cycle. The terms on the right-hand-side represent the energy sinks and loss mechanisms: reradiation from the solar cavity ($q_{\text{reradiation}}$), convective losses from the reactor to the ambient (q_{loss}), sensible heating of the sweep gas (q_{sg}), sensible heating of the oxidant (q_{ox}), and finally, the energy required to drive the dissociation of CO_2 (q_{chem}). Reradiation is modeled assuming that the cavity is effectively black,

$$q_{\mathrm{reradiation}} = \frac{\sigma T_{\mathrm{R}}^4}{CI} q_{\mathrm{solar}}, \tag{3.7}$$

where the concentration ratio, C, depends on the optical design of the concentrating facility and the geometry of the reactor aperture. In the present study, C = 3000, a level attainable with state-of-the-art parabolic dish optics [1] and favorable for operation at 1500 °C [6]. Convective losses are treated as a fraction of the solar energy not lost to reradiation,

$$q_{\mathrm{loss}} = F(q_{\mathrm{solar}} - q_{\mathrm{reradiation}}). \tag{3.8}$$

Here F = 0.2, consistent with reported values for solar reactors [31]. The fractions of heat recuperated to preheat the sweep gas and oxidant flows are assumed equal. The sensible heat load of the sweep gas is given by

$$q_{\mathrm{sg}} = \frac{\dot{n}_{\mathrm{sg}}}{m_{\mathrm{CeO_2}}} \left(\frac{\tau_{\mathrm{rd}}}{\tau_{\mathrm{rd}} + \tau_{\mathrm{ox}}}\right) \left[\bar{h}_{\mathrm{sg}}(T_{\mathrm{R}}) - \bar{h}_{\mathrm{sg}}(T_{\mathrm{sg,out}})\right], \tag{3.9}$$

where $\dot{n}_{\mathrm{sg}}$ is the molar flow rate of sweep gas and $T_{\mathrm{sg,out}}$ is the temperature of the sweep gas leaving the heat recuperator, calculated as a function of recuperator effectiveness. The effectiveness is defined as the ratio of sensible heat recuperated to the maximum that could be recuperated. In the case of reduction,

$$\epsilon = \frac{\bar{h}_{\mathrm{sg}}(T_{\mathrm{sg,out}}) - \bar{h}_{\mathrm{sg}}(T_{\mathrm{amb}})}{\bar{h}_{\mathrm{sg}}(T_{\mathrm{R}}) - \bar{h}_{\mathrm{sg}}(T_{\mathrm{amb}})}. \tag{3.10}$$

The sensible heat load of the oxidant is given by

$$q_{\mathrm{ox}} = \frac{\dot{n}_{\mathrm{ox}}}{m_{\mathrm{CeO_2}}}\left(\frac{\tau_{\mathrm{ox}}}{\tau_{\mathrm{rd}} + \tau_{\mathrm{ox}}}\right)\left[\bar{h}_{\mathrm{ox}}(T_{\mathrm{R}}) - \bar{h}_{\mathrm{ox}}(T_{\mathrm{ox,out}})\right], \tag{3.11}$$

where $\dot{n}_{\mathrm{ox}}$ is the molar flow rate of oxidant and $T_{\mathrm{ox,out}}$ is the temperature of the oxidant leaving the recuperator. The energy required to produce the fuel is given by

$$q_{\mathrm{chem}} = \overline{\dot{n}_{\mathrm{CO}}'} \times \Delta_{\mathrm{r}}H|_{T_{\mathrm{R}}}\,, \tag{3.12}$$

where $\overline{\dot{n}_{\mathrm{CO}}'}$ is the rate of fuel production per unit mass of ceria and $\Delta_{\mathrm{r}}H$ is the enthalpy change of the dissociation of CO_2 with all species at the operating temperature, calculated by

$$\Delta_{\mathrm{r}}H|_{T_{\mathrm{R}}} = \bar{h}_{\mathrm{CO}}(T_{\mathrm{R}}) + \frac{1}{2}\bar{h}_{\mathrm{O_2}}(T_{\mathrm{R}}) - \bar{h}_{\mathrm{CO_2}}(T_{\mathrm{R}}). \tag{3.13}$$

The exothermic energy release during oxidation is assumed to be transferred within a continuous-operation solar reactor to offset the endothermic energy of oxygen vacancy formation.

3.2 Results and Discussion

3.2.1 Selection of Flow Rate and Cycling Period

An example isothermal redox cycle at 1500 °C is shown in Figure 3.5. The general behavior is typical of all flow rates considered. Initially, the ceria is in equilibrium with a 100% CO_2 gas atmosphere such that its non-stoichiometry is $\delta_{\mathrm{eq}} = 0.021$. At $t = 0$, sweep gas is injected at a flow rate of 581 mL min^{-1} g^{-1}. Oxygen is released immediately at a rate of 0.50 μmol s^{-1} g^{-1}. The rate decays as the number of oxygen vacancies in the ceria approaches $\delta = 0.060$ corresponding to the new equilibrium state of ceria. At t = 21 min, oxidation is initiated by replacing the sweep gas flow with a 297 mL min^{-1} g^{-1} flow of CO_2. Carbon monoxide production rises rapidly and peaks at a value of 2.2 µmol s^{-1} g^{-1} just 0.15 min after CO_2 injection. It then decays to a steady rate of 0.47 µmol s^{-1} g^{-1} at t = 25 min. Simultaneously, the O_2 production rate rises from zero to a steady 0.24 µmol s^{-1} g^{-1}. The observation of steady production of O_2 and CO from a stream of 100% CO_2 reflects quenching of the thermolysis reaction, where the latter occurs independently of the presence of ceria. Such behavior is primarily an artifact of the rapid cooling of the product gases in the flow passage from the furnace to the gas analyzer, and has also been observed during isothermal hydrogen production [21]. Without such a rapid quench, the O_2 and CO produced by thermolysis would recombine. Consequently, the products of CO_2 thermolysis are excluded from the reported production rate data.

Figure 3.6 shows the impact of sweep gas flow rate on the transient rate of production of O_2. Two important trends are evident. First, for each flow rate considered, the rate of production is fastest at the beginning of the reduction period. Second, the rate increases as the flow rate is increased from 50 to 300 mL min^{-1} g^{-1} and then remains nearly constant from 300 to 600 mL min^{-1} g^{-1}. The latter trend is illustrated by an inset plot of the O_2 production rate averaged over the first four minutes of reduction. These results suggest that the rate is gas-phase mass transport limited for flow rates less than 300 mL min^{-1} g^{-1} and limited by the surface reaction kinetics of the material at higher flow rates.

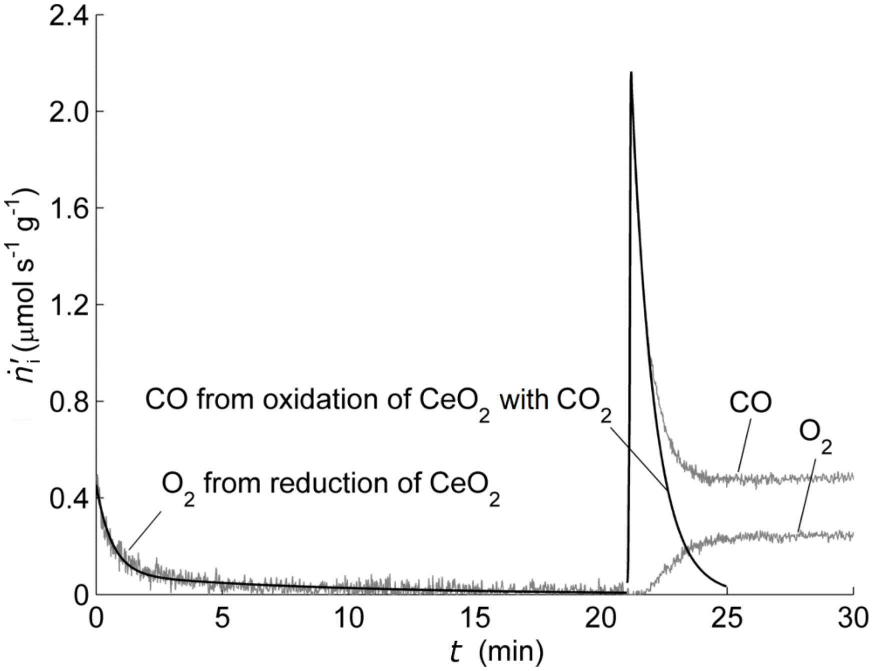

Figure 3.5 A typical isothermal pressure-swing cycle at 1500 °C in the porous pellet bed reactor. The sweep gas flow rate is 581 mL min^{-1} g^{-1} and the CO_2 flow rate is 297 mL min^{-1} g^{-1}. Smoothed data (black lines) eliminate instrument noise; the smoothed CO production excludes CO_2 thermolysis products.

Figure 3.7a shows the impact of the CO_2 flow rate on the transient rate of CO production, and Figure 3.7b shows the production rate averaged over the first 90 s. Similar to the trends presented for reduction, production rates increase with increasing flow rate up to 300 mL min^{-1} g^{-1} and then remain constant. Oxidation is gas-phase mass transport limited below 300 mL min^{-1} g^{-1} and limited by material kinetics at higher flow rates. In isothermal H_2O-splitting, the rate of H_2 production was doubled in the presence of Rh catalyst, which corroborates our observation of a surface reaction limited regime in the oxidation step [21].

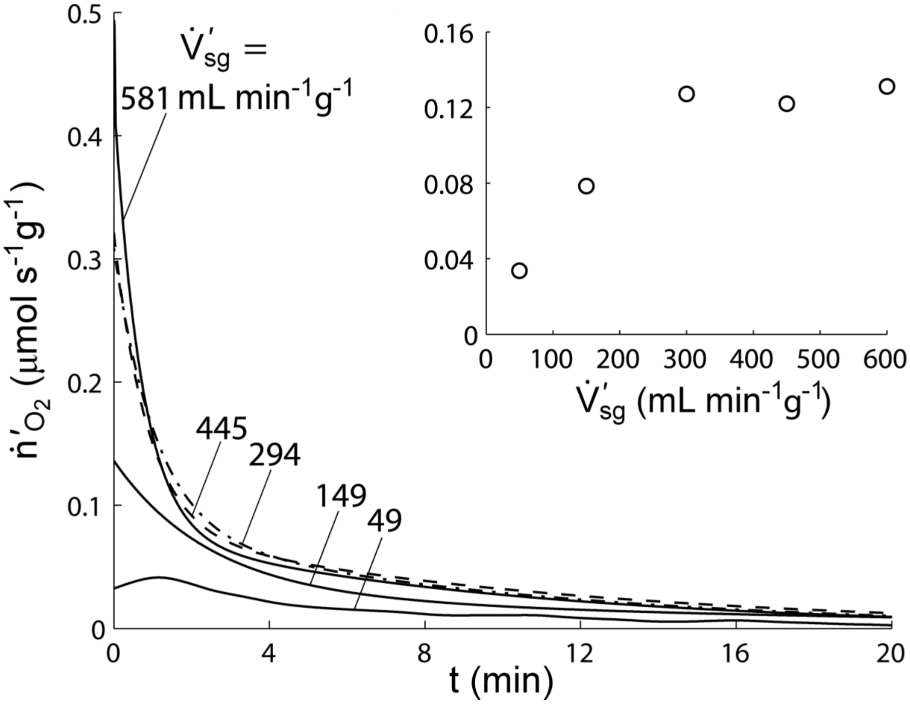

Figure 3.6 Transient global rates of O_2 production during reduction at 1500 °C for sweep gas flows of 50–600 mL min^{-1} g^{-1}. Inset: the average rate versus flow rate for the first 4 minutes of reduction.

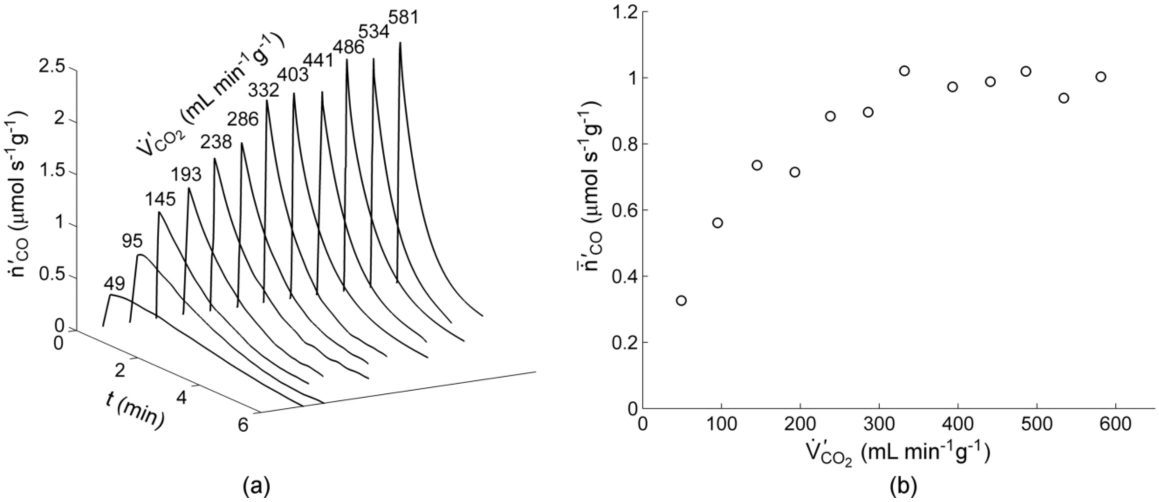

Figure 3.7 (a) Transient global rates of CO production during oxidation at 1500 °C for CO_2 flow rates of 50–600 mL min^{-1} g^{-1} and (b) the average rate over the first 90 s.

Together, Figures 3.6 and 3.7 imply that sweep gas and CO_2 flow rates above 300 mL min^{-1} g^{-1} are unfavorable for isothermal cycle operation. Above 300 mL min^{-1} g^{-1}, there is no gain in the rate of O_2 release and CO production, but there are penalties due to the loss of energy to heat the gases, increased pumping power, and the increased cost of supplying inert sweep gas and oxidizer. The question then arises: what are the flow rates and durations of reduction and oxidation that optimize the cycle with respect to efficiency? To answer this question, one must consider the effects of flow rate and duration of reduction and oxidation on the rate of fuel production and the process efficiency, as expressed in equation (3.5). Here we focus on optimization of efficiency at 1500 °C assuming 90% heat recovery effectiveness, 3000 suns concentration, and 20% reactor losses. In anticipation of scaling the results to a reactor in which extremely short cycle times are impractical, the cycling period is constrained to a minimum of four minutes.

With this constraint, application of the optimization procedure described in Section 3.1.3 of this thesis was applied to all flow rates to determine the optimum combination of flow rates and reduction and oxidation periods that maximizes efficiency. The optimal combination is a sweep gas flow of 150 mL min^{-1} per gram of ceria and a CO_2 flow of 50 mL min^{-1} per gram of ceria with reduction and oxidation periods of 100 s and 155 s, respectively. For these conditions, the *predicted* average CO production rate is 0.075 µmol s^{-1} g^{-1} and the corresponding projected efficiency is 3.7%. The predicted efficiency falls between the estimates obtained in prior thermodynamic analysis depending on the assumptions for gas flow rates [20]. With the identical assumptions of

90% heat recovery effectiveness, 3000 suns concentration, and 20% reactor losses, the thermodynamic limit for efficiency is 11% for a counter-current flow arrangement of gas and ceria and 0.01% for a mixed-flow arrangement. The fact that the projected efficiency in the present analysis is orders of magnitude higher than for the worse case of mixed-flow indicates that flow through the packed bed minimizes back-mixing, reducing the required flow of sweep gas and CO_2. The projected efficiency is 34% of the maximum efficiency for counter-flow of sweep and oxidizing gases. Alternating the gas flow direction may further reduce the required gas flow rates. However, alternating gas flows introduces practical challenges for the design of an effective heat recuperation system. Another option for increasing efficiency is to use an inert sweep gas with a lower specific heat than N_2, for example, Ar. Lowering the specific heat of the sweep gas is equivalent to a corresponding reduction in mass flow rate.

For the optimum gas flow rates, Figure 3.8 illustrates how the fraction of the cycle allotted for reduction can be tailored for a fixed cycle duration to either maximize efficiency *or* the rate of CO production. Because of the greater thermal capacity of the sweep gas flow relative to the CO_2 flow, the reduction period for maximum efficiency is shorter than for maximum fuel production. Shorter reduction periods minimize sensible heating and provide a modest improvement in efficiency despite a small reduction in CO production rate. The figure also illustrates the penalty of selecting non-optimum reduction and oxidation periods. If less than ~30% of the cycle is spent on reduction or oxidation, the fuel production rate declines dramatically, and efficient fuel production is not possible.

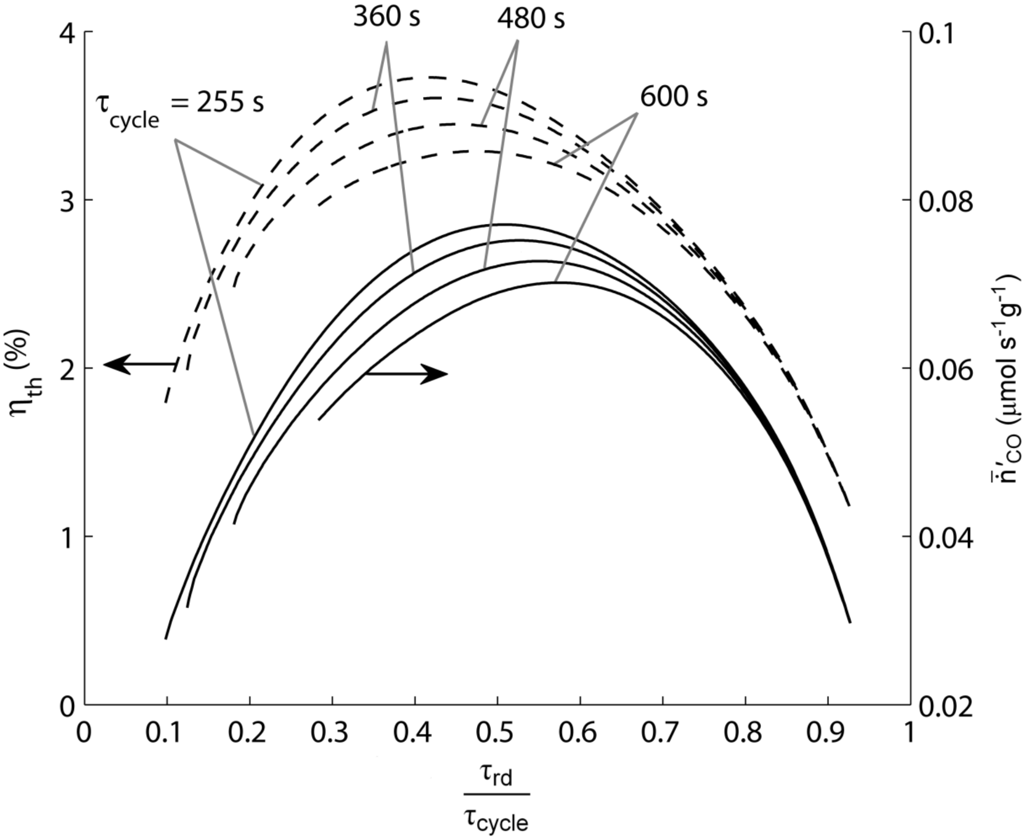

Figure 3.8 The projected thermal efficiency and the average rate of CO production with sweep gas and CO_2 flow rates of 150 mL min^{-1} g^{-1} and 50 mL min^{-1} g^{-1} and with cycle durations from 255–600 s versus the fraction of the cycle duration allotted for reduction. Projected efficiency is based on 90% gas phase heat recovery, a concentration ratio of 3000, and convective losses of 20%.

Figure 3.9 highlights the importance of gas phase recovery and its impact on the tradeoff in fuel production and efficiency. The efficiency and the average rate of CO production are shown for CO_2 flow rates from 50 to 300 mL min^{-1} g^{-1} and for gas phase sensible heat recuperation from 0 to 95%. For each datum, the sweep gas flow rate and cycle duration are optimized (the optimized values are not indicated for visual clarity). For CO_2 flow rates less than 300 mL min^{-1} g^{-1}, oxidation is gas-phase mass-transport limited, and the rate of CO production increases with CO_2 flow rate. However, this increase is not enough to offset the corresponding increase in sensible heating, resulting in lower thermal efficiency regardless of the level of heat recuperation for the levels depicted in Figure 3.9. Without heat recuperation, the projected efficiency is less than 0.5%. For plausible, but aggressive, levels of heat recuperation of 70%, 80%, 90%, and 95%, the efficiency increases to 1.5%, 2.0%, 3.7%, and 6.9% at a CO_2 flow rate of 50 mL min^{-1} g^{-1}. There is minimal improvement in process efficiency for heat recuperation of less than ~70% because the sensitivity of the efficiency to heat recuperation increases with effectiveness. The development of highly effective heat exchangers that operate at the elevated temperatures required for the reduction of ceria is thus crucial for efficient fuel production.

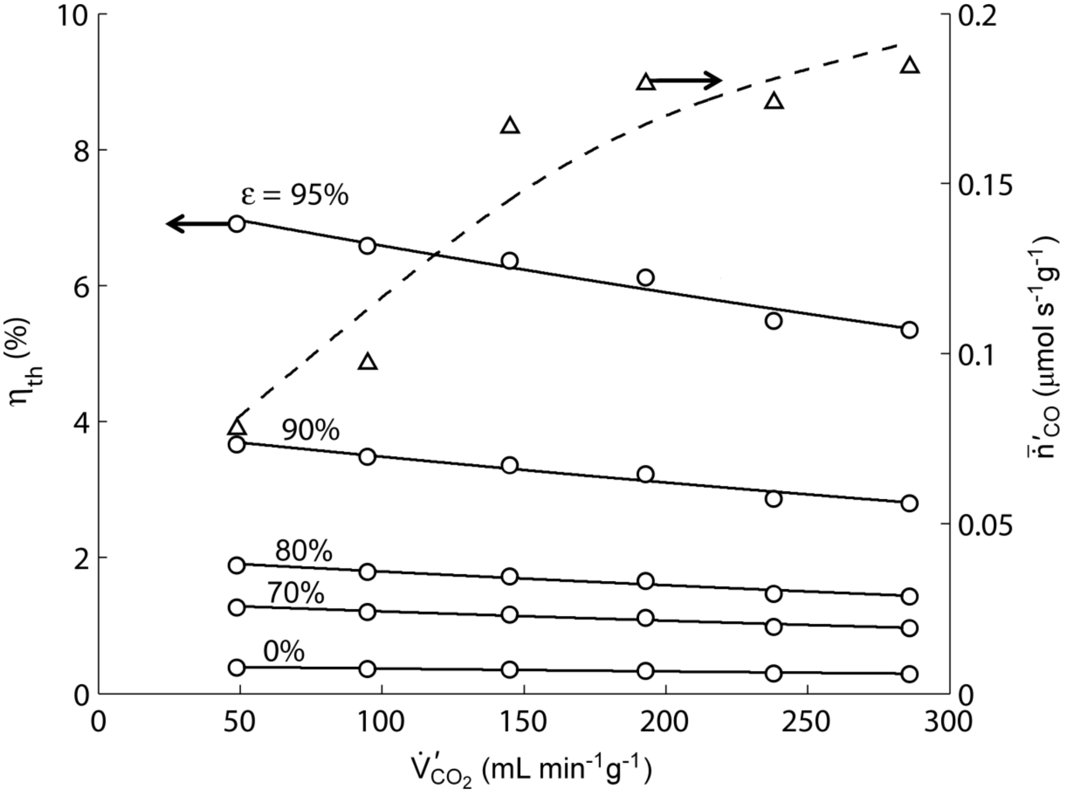

Figure 3.9 The projected efficiency (circles, solid lines) and average CO production rate (triangles, dashed line) with the optimum reduction and oxidation periods and sweep gas flow rate for CO_2 flows between 50 and 300 mL min^{-1} g^{-1}. Gas phase heat recovery (ε) is varied from 0–95%. Projected efficiency is based on a concentration ratio of 3000 and convective losses of 20%.

3.2.2 Demonstration of Optimum Isothermal Cycling

To demonstrate the utility of the optimization strategy and the stability of CO production over the packed bed of porous ceria pellets, the optimum cycling conditions were implemented for 102 consecutive cycles (Figure 3.10). The rates of production and the total CO and O_2 produced are stable within experimental uncertainty (±0.2 μmol g^{-1}), and occur in a 2:1 ratio. These features indicate that all oxygen vacancies formed during reduction are utilized for the production of CO and that ceria sublimation under these conditions is negligible. For 1500 (±11) °C, the average rate of CO production is 0.079 (±0.0005) μmol s^{-1} g^{-1}, close to the rate predicted by the optimization analysis (0.075 μmol s^{-1} g^{-1}). The average rate of CO production *achieved* in the 102 cycles corresponds to a projected process efficiency of 4.0% assuming 90% heat recovery effectiveness, 3000 suns concentration, and 20% reactor losses.

A representative cycle is shown on the inset of Figure 3.10. The data reflect the optimized nature of the cycle as there is little decay in the rates of reduction and oxidation during cycling, an important feature for achieving high average rates of fuel production. The rate of O_2 release during reduction reaches a peak of 0.10 μmol s^{-1} g^{-1} and declines to 0.08 μmol s^{-1} g^{-1} over the 100 s reduction. Similarly, the rate of CO production reaches a maximum of 0.16 μmol s^{-1} g^{-1} and declines to 0.13 μmol s^{-1} g^{-1}. Under these optimized conditions, CO represents 0.4% of the product stream during oxidation (equal to the percent conversion of CO_2) and O_2 represents 0.09% of the product stream during reduction. The thermal equivalent minimum energies required to separate the CO and O_2 from their respective gas streams at 25 °C assuming a 35% efficient heat-to-work conversion ($T\Delta S_{\text{mix}}/\eta$) are 0.94 J cycle^{-1} g^{-1} and 0.51 J cycle^{-1} g^{-1}, respectively. The solar thermal input to the cycle is 143 J cycle^{-1} g^{-1}. Including the separation term in the denominator of the efficiency calculation (equation (3.5)) decreases the projected efficiency by ~0.01%. Thus, while efficient separation is important for efficient fuel production, its impact on process efficiency is small compared to the other factors discussed in the present study, including effective heat recovery. Separation is more likely to be an economic challenge than one of energy penalties.

When compared to temperature-swing operation, isothermal operation of the ceria redox cycle provides equally attractive rates of fuel generation. The average rate of fuel production in the temperature-swing ceria-based cycle operating at 1500 °C during reduction and at 800 °C during oxidation has been estimated to be 0.093–0.15 μmol g^{-1} s^{-1} [21]. The 0.079 μmol g^{-1} s^{-1} rate of CO production achieved isothermally is 85% of the rate predicted for the temperature-swing cycle, a significant result given that isothermal operation eliminates the need for solid-state heat recuperation to simplify high-temperature solar reactor construction.

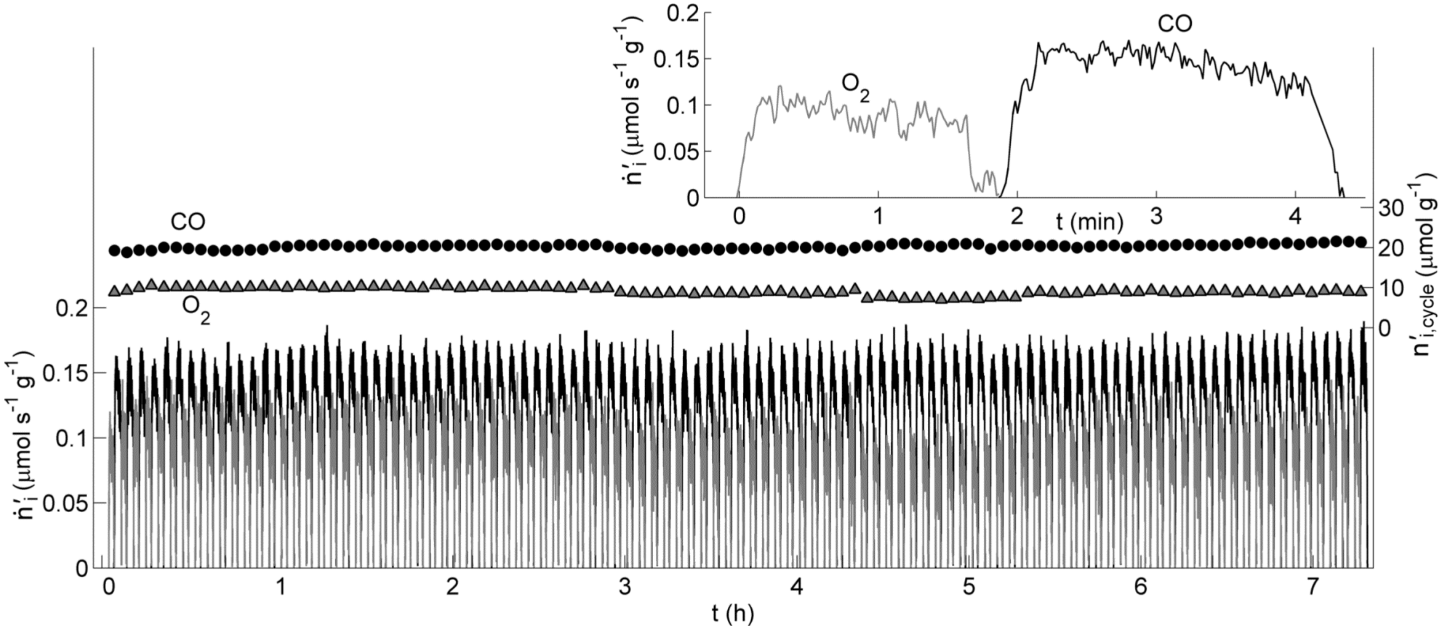

Figure 3.10 The transient rates of O_2 and CO production and the total O_2 and CO produced in 102 cycles completed with the optimized flow rates of 150 mL min^{-1} g^{-1} sweep gas and 50 mL min^{-1} g^{-1} CO_2 and cycling periods of 100 s and 155 s for reduction and oxidation, respectively. The inset depicts the transient rates of O_2 and CO production in cycle 80.

3.2.3 Scale Up for a Prototype Solar Reactor

While the optimum cycling parameters were identified and demonstrated in the laboratory, similitude shows that the results scale to larger prototypes. The laboratory results thus avoid the need for costly on-sun testing aimed at identifying operational parameters of larger prototype reactors. Similitude also justifies the earlier analysis of the cycle solar energy balance on a unit mass basis (equation (3.6)).

The similarity parameters for the pellet bed, derived from a dimensional analysis of the volume-averaged conservation of fluid species (see Appendix A), are the Peclet number, the Damköhler number, and the aspect ratio. The aspect ratio is the ratio of the length to the radius of the pellet bed,

$$\Gamma = \frac{L}{R_{\mathrm{bed}}}. \tag{3.14}$$

The Peclet number,

$$Pe_{\mathrm{L}} = \frac{UL}{\mathcal{D}_{\mathrm{i,eff}}}, \tag{3.15}$$

is the ratio of the characteristic time of gas diffusion to the mean gas residence time. The Damköhler number,

$$Da = \frac{L/U}{c_{\mathrm{f}}^{o}/\dot{n}''_{\mathrm{i,ref}}a}, \tag{3.16}$$

is the ratio of the mean gas residence time to the characteristic reaction time. The reference reaction rate, $\dot{n}''_{\mathrm{i,ref}}$, is traditionally evaluated at the inlet of the pellet bed using an analytic expression for the surface kinetics, e.g., that by Bulfin *et al.* [32]. However, kinetics are intrinsic to the composition and morphology of the pellets, which fixes the characteristic reaction time in the pellet bed. Thus, if the morphology and size of the pellets are the same at both scales, the only requirement to scale the Damköhler number is to scale the gas flow rates to match the gas residence time in the pellet bed. To do so, the sweep gas and CO_2 flow rates must increase in proportion to the ceria mass because the mass of ceria in the pellet bed is proportional to its length and the gas flow rate is proportional to the velocity,

$$\frac{L}{U} \propto \frac{m_{\mathrm{CeO_2}}}{\dot{n}_{\mathrm{i}}} \tag{3.17}$$

(where species i is either sweep gas or CO_2). This scaling law motivated an energy balance of the cycle on a unit mass basis (equation (3.6)). Note that similarity of both the Peclet and Damköhler numbers cannot be achieved because the Peclet number is proportional to and the Damköhler number is inversely proportional to gas velocity. However, as shown in Appendix A, if the species mole fractions are uniform in the radial direction and if the Peclet number is large, only the Damköhler number must be matched to ensure similarity.

To demonstrate the flow rate scaling law in equation (3.17), the conditions identified to maximize efficiency at 1500 °C in the small-scale, 1 gram pellet bed reactor were scaled up for a pellet bed reactor containing 22 grams of ceria and operated in the cavity of a solar receiver (see Ref. [28]). The aspect ratios in the 1 gram and 22 gram pellet beds were 2.1 and 6.4, respectively; the Peclet numbers during reduction and oxidation in the 1 gram and 22 gram pellet beds were 5 and 12 and 120 and 310, respectively. The average rate of CO production obtained is 0.069 μmol s^{-1} g^{-1}, 13% lower than the average rate of CO production measured in the 1 gram pellet bed. Despite a three-fold difference in the aspect ratio and a factor of ~20 difference in the Peclet numbers, scaling the gas flow rates on the ceria mass yielded similar Damköhler numbers and hence similar average rates of CO production and projected efficiency.

3.3 Summary and Conclusions

This study demonstrates an isothermal thermochemical cycle to split CO_2 based on non-stoichiometric reduction and oxidation of ceria. Fuel production rates are measured at 1500 °C for a bed of porous pellets by alternating between a flow of inert sweep gas and a flow of CO_2. Gas flow rates are varied from 50 to 600 mL min^{-1} g^{-1}. The data elucidate the tradeoff between the requirement for a sufficiently high flow of sweep gas and CO_2 to overcome gas-phase mass transport-limited rates of fuel production and the requirement to heat the gases to the reaction temperature. This tradeoff is a crucial consideration in the selection of gas flow rates and reduction and oxidation periods for efficient conversion of sunlight to chemical energy in a solar reactor.

A new approach is taken to predict the efficiencies for ceria-based thermochemical cycles. Prior studies assume thermodynamic fuel production. In a real reactor subject to finite rates of reaction, the upper limit of thermodynamic productivity can only be reached with long cycle times accompanied by low average rates of fuel production. We provide a procedure for optimizing the efficiency based on selection of flow rates and reduction and oxidation periods using laboratory scale data. The results advocate short cycle times and flow rates less than 300 mL min^{-1} g^{-1} of ceria with high levels (~90%) of gas phase heat recovery. By applying the principle of similitude, the results can be scaled to a solar reactor by matching the flow rates in proportion to the ceria mass.

Based on the data, the recommended operating conditions are a flow rate combination of 150 mL min^{-1} g^{-1} sweep gas and 50 mL min^{-1} g^{-1} CO_2 flow with reduction and oxidation periods of 100 s and 155 s, respectively. As demonstrated in the porous pellet bed for 102 stable cycles over 7.25 h, these operating conditions yield an average CO production rate of 0.079 μmol s^{-1} g^{-1} and a projected process efficiency of 4.0% assuming 90% heat recovery effectiveness, 3000 suns concentration, and 20% reactor heat losses; the measured rate of CO production agrees with the value of 0.075 μmol s^{-1} g^{-1} predicted from the optimization analysis. More rapid CO production is possible with higher gas flow rates, but only at the expense of reduced efficiency. Sensible heating of the gases is a major thermal loss. Thus efforts to reduce the sweep gas and CO_2 flows without loss of fuel productivity will have high payoff in terms of increased efficiency. Furthermore, development of gas phase heat recovery systems at the elevated temperature required for the ceria cycle is imperative.

4 Quasi-Equilibrium Limit of Reaction Rates

In Chapter 3, experimental data for isothermal CO_2 splitting in a bed of porous ceria pellets showed that at sweep gas and oxidizer flow rates greater than ~300 mL min^{-1} g^{-1}, the rates of reduction and oxidation are insensitive to the flow rates, suggesting that the surface reactions are rate limiting. Below flow rates of 300 mL min^{-1} g^{-1}, however, reaction rates are sensitive to the flow rates of sweep gas and oxidizer, indicating that mass transfer limits the reaction rates. The Wagner Modulus for the porous pellets was less than 0.15, so diffusion of the gaseous reactants and products through the pores of the ceria pellets is not rate limiting; furthermore, the small solid feature sizes, together with the high diffusivity of oxygen through solid ceria, make it unlikely that oxygen diffusion will limit the rates of reaction (see Section 3.1.1 and Ref [2]). Studies on temperature swing ceria cycling have suggested that heat transfer is rate limiting for reduction [10,11,15], but isothermal cycling has no temperature change between oxidation and reduction, making a heat transfer limitation unlikely.

In this chapter, I develop a model which assumes that the surface reaction, heat transfer, diffusion of reactants and products, mass transfer from pellet surface to the free stream, and the CO_2 dissociation reaction (for oxidation) are all very fast—so fast that the ceria remains in a state of quasi-equilibrium with the surrounding gas atmosphere. In this physical situation, the gas flow over the ceria reaches the maximum (for reduction) or minimum (for oxidation) possible O_2 partial pressure; this limiting p_{O_2} is defined by ceria equilibrium thermodynamics as a function of temperature and non-stoichiometry (see Figure 2.1) [9]. A similar quasi-equilibrium assumption for the reduction of ceria was made by Keene *et al.* in Ref. [33], where the authors set a parameter in their kinetic expression for ceria reduction to be sufficiently large that quasi-equilibrium is maintained.

With a known gas flow rate and total pressure, the p_{O_2} found under the quasi-equilibrium assumption can be converted into an O_2 production rate in the case of reduction and an O_2 consumption rate (and corresponding CO production rate) in the case of oxidation. These rates represent upper limits for the reduction and oxidation rates—that is, they are the rates that are achieved in the absence of all other potential limitations (e.g. oxygen bulk diffusion, surface kinetics, diffusion through pores, etc.). With a favorable ceria morphology (which prevents rate limitations by oxygen bulk diffusion and gaseous diffusion through pores) and over a certain range of gas flow rates (low enough that all other potentially limiting processes can reach equilibrium during the gas residence time over the ceria), the quasi-equilibrium model is found to accurately describe experimental data.

A quasi-equilibrium model of O_2 and CO production rates is first developed and then compared with experimental data.

4.1 Quasi-Equilibrium Model of Isothermal Reaction Rates

For a given isothermal temperature, the thermodynamics of ceria provides p_{O_2} as a function of δ. In this model, the bed of ceria pellets is treated as spatially uniform in δ (i.e. gradients in δ are ignored)[8]. Under the quasi-equilibrium assumption, the sweep gas exiting the bed of ceria pellets has the equilibrium p_{O_2} corresponding to the ceria's δ. Assuming a total pressure of 1 atm, the mole fraction of O_2 in the sweep gas is calculated from p_{O_2} as a function of δ.

The mole fraction of O_2 in the sweep gas leaving the ceria can also be expressed by the definition of mole fraction as

$$x_{O_2,out,rd} = \frac{\dot{n}_{O_2,in} + r_{O_2}}{\dot{n}_{O_2,in} + \dot{n}_{N_2} + r_{O_2}}, \tag{4.1}$$

where $\dot{n}_{O_2,in}$ is the trace flow rate of O_2 entering the bed as the result of impurities in the sweep gas, $\dot{n}_{N_2}$ is the flow rate of N_2, and r_{O_2} is the rate of O_2 production within the bed of ceria pellets. All rates are evaluated per unit mass of ceria. Solving for r_{O_2} and recognizing that $x_{O_2,out,red}$ is known as a function of δ from ceria thermodynamics,

$$r_{O_2}(\delta) = \frac{x_{O_2,out,rd}(\delta) \cdot \left(\dot{n}_{O_2,in} + \dot{n}_{N_2}\right) - \dot{n}_{O_2,in}}{1 - x_{O_2,out,rd}(\delta)}. \tag{4.2}$$

The rate of O_2 production is directly proportional to the rate of change of ceria non-stoichiometry:

---

[8] To capture the effects of gradients in δ, this model could be applied to a domain that is discretized along the direction of gas flow.

$$r_{O_2}\left[\frac{mol\ O_2}{s\cdot g\ ceria}\right]=\frac{1}{2}\left[\frac{mol\ O_2}{mol\ vac}\right]\frac{1}{M_{CeO_2}}\left[\frac{mol\ ceria}{g\ ceria}\right]\frac{d\delta}{dt}\left[\frac{\frac{mol\ vac}{mol\ ceria}}{s}\right], \tag{4.3}$$

or

$$r_{O_2}=K\frac{d\delta}{dt}, where\ K=2.905\times10^{-3}\ \left[\frac{mol\ O_2\cdot mol\ ceria}{mol\ vac\cdot g\ ceria}\right], \tag{4.4}$$

where "vac" indicates oxygen vacancies. Recalling that $r_{O_2}$is known as a function of δ from equation (4.2), equation (4.4) is separated and integrated:

$$\int_0^t d\hat{t}=\int_{\delta_{ox}}^{\delta}\frac{K}{r_{O_2}(\hat{\delta})}d\hat{\delta}, \tag{4.5}$$

where the "hat" symbol (^) denotes a variable of integration and δ_{ox} is the non-stoichiometry at $t=0$. Equation (4.5) provides a relation between δ and t, which can be used to find $\frac{d\delta}{dt}$ and, via equation (4.4), the O_2 production rate as a function of time.

A similar procedure is employed for oxidation, although the dissociation of CO_2, which is significant at the high oxidation temperatures encountered in isothermal cycling[9], adds some complexity to the calculation of equilibrium p_{O_2}. For the CO_2 dissociation reaction,

$$CO_2\rightleftharpoons CO+\frac{1}{2}O_2, \tag{4.6}$$

the equilibrium condition is expressed as

---

[9] Pure CO_2 at ambient temperature will become 0.4% CO and 0.2% O_2 in equilibrium at 1500 °C.

$$K_{eq}(T) = \frac{\dot{n}_{CO}^{o} + \xi}{\dot{n}_{CO_2}^{o} - \xi}\left(\frac{\dot{n}_{O_2}^{o} + \frac{1}{2}\xi - r_{O_2,sink}}{\sum(\dot{n}_i^o) + \frac{1}{2}\xi - r_{O_2,con}} p_{tot}\right)^{\frac{1}{2}}, \tag{4.7}$$

where $K_{eq}(T)$ is the temperature-dependent equilibrium constant; $\dot{n}_{CO_2}^{o}$, $\dot{n}_{CO}^{o}$, and $\dot{n}_{O_2}^{o}$ are the initial flow rates of the species; $\sum(\dot{n}_i^o)$ is the initial flow rate of all species; ξ is the rate of the dissociation reaction (i.e. the number of moles per second of CO_2 that dissociate); and $r_{O_2,sink}$ is an O_2 sink used to account for the gaseous oxygen which is consumed via the oxidation of ceria[10]. Using the same notation, the mole fraction of O_2 after oxidation is

$$x_{O_2,out,ox} = \frac{\dot{n}_{O_2}^{o} + \frac{1}{2}\xi - r_{O_2,sink}}{\sum(\dot{n}_i^o) + \frac{1}{2}\xi - r_{O_2,sink}}, \tag{4.8}$$

where, under the quasi-equilibrium assumption, $x_{O_2,out,ox}$ is known as a function of δ from the thermodynamics of ceria (at fixed values of isothermal temperature and total pressure).

For each δ of interest, equations (4.7) and (4.8) are solved simultaneously for ξ and $r_{O_2,sink}$. Note that, as compared to reduction, applying the quasi-equilibrium model to oxidation requires the additional assumption that the rate of the CO_2 dissociation reaction is fast compared to the rate that products are swept away from the ceria by the oxidizing gas flow.

As the product stream cools to ambient temperature, the CO originating from the CO_2 dissociation recombines with the remaining O_2 (i.e. the O_2 produced by CO_2

---

[10] A similar approach to account for both oxidizer dissociation and the oxidation reaction was used in Ref. [20].

dissociation that was *not* consumed in the oxidation of ceria), using up nearly all the O_2; the remaining CO is the fuel produced by the cycle. Using the stoichiometry of equation (4.6), the fuel production rate is twice the O_2 consumption rate,

$$r_{CO}(\delta) = 2r_{O_2,sink}(\delta). \tag{4.9}$$

Analogous to equation (4.4), the CO production rate can be related to the rate of change of δ:

$$r_{CO} = -2K\frac{d\delta}{dt}. \tag{4.10}$$

Separating and integrating equation (4.10) yields

$$\int_0^t d\hat{t} = \int_{\delta_{ox}}^{\delta} \frac{-2K}{r_{CO}(\hat{\delta})} d\hat{\delta}. \tag{4.11}$$

Solving equation (4.11) provides a relation between δ and time, which can then be used with equation (4.10) to find the rate of CO production in time, under the assumption that quasi-equilibrium is maintained between the ceria and oxidizing gas flow. The quasi-equilibrium models for both reduction and oxidation were implemented in MATLAB (version 2013a).

This quasi-equilibrium model has a few limitations. First, it only applies when all other potentially limiting processes (e.g. oxygen bulk diffusion, surface kinetics, diffusion through pores, etc.) are sufficiently fast. Thus, it can only describe ceria with small solid feature sizes (to prevent bulk oxygen limitations) and quick gaseous diffusion through internal pores. In addition, since the quasi-equilibrium predicts the O_2 or CO production rates to increase with the total gas flow rates, it is reasonable to expect that quasi-equilibrium may apply at low flow rates, but as the flow rate increases, there will come a point where the quasi-equilibrium production rates exceed the rates of another process such as the surface reaction, and the quasi-equilibrium model will no longer apply. Another limitation of this model is the assumption that there are no spatial gradients in either δ or temperature. These assumptions are acceptable for short pellet beds such as the 10 mm long packed bed used for experiments in the IR furnace. For modeling much longer beds, where gradients in δ may be significant, or to capture the effects of temperature gradients, the ceria pellet bed could be discretized in the axial direction.

4.2 Isothermal Model Results and Discussion

Figures 4.1 and 4.2 compare the quasi-equilibrium model to experimental data for isothermal reduction of a bed of porous ceria pellets at 1500 °C with an inlet sweep gas p_{O_2} of 10^{-5} atm (i.e. the same reduction data reported in Chapter 3)[11]. The initial state for both the model and the experiment is equilibrium under 100% CO_2 at 1500 °C. Figure 4.1 shows results with sweep gas flow rates of 50, 150, 300, 450, and 600 mL min^{-1} g^{-1}, while Figure 4.2 shows the first 3 minutes of reduction for 50, 300, and 600 mL min^{-1} g^{-1}. Note that in Figure 4.1, the quasi-equilibrium model results are only shown for the length of time over which experimental data were taken, but the model predicts O_2 production to continue indefinitely as the O_2 production rate asymptotically approaches zero. The integrated total O_2 production in one cycle predicted by the model agrees with the predictions from ceria thermodynamics.

---

[11] All volumetric gas production rates reported in this chapter are evaluated at the reference conditions of 25 °C, 1 bar.

The model is in close agreement with the measured rates for sweep gas flows of 300 mL min^{-1} g^{-1} or less. At flows greater than 300 mL min^{-1} g^{-1}, the quasi-equilibrium model over-predicts the O_2 production at the beginning of reduction, consistent with the conclusion in Chapter 3 that the surface reaction plays a role in determining the rate of reduction at these flow rates. The consistency between the model and experimental data for flow rates $\leq$ 300 mL min^{-1} g^{-1} (i.e. the same range over which average O_2 production rates were found in Chapter 3 to be sensitive to sweep gas flow rate) strongly suggests that quasi-equilibrium between the ceria and sweep gas is the mechanism responsible for limiting the isothermal reduction rates in the porous ceria pellet bed over this range of sweep gas flow rates.

Figures 4.3 and 4.4 compare the results of the quasi-equilibrium model and experimental data for isothermal oxidation at 1500 °C with 100% CO_2 (again, data are from Chapter 3). For each gas flow rate, the initial non-stoichiometry was chosen to match that of the experimental data, calculated from the total CO production of the cycle. The model closely matches the experimental results at the lowest flow rates, but the model deviates from the experimental results at flow rates above ~150 mL min^{-1} g^{-1}. Note that the model is not expected to apply at flow rates higher than ~300 mL min^{-1} g^{-1}, where the surface reaction limits the rate of oxidation.

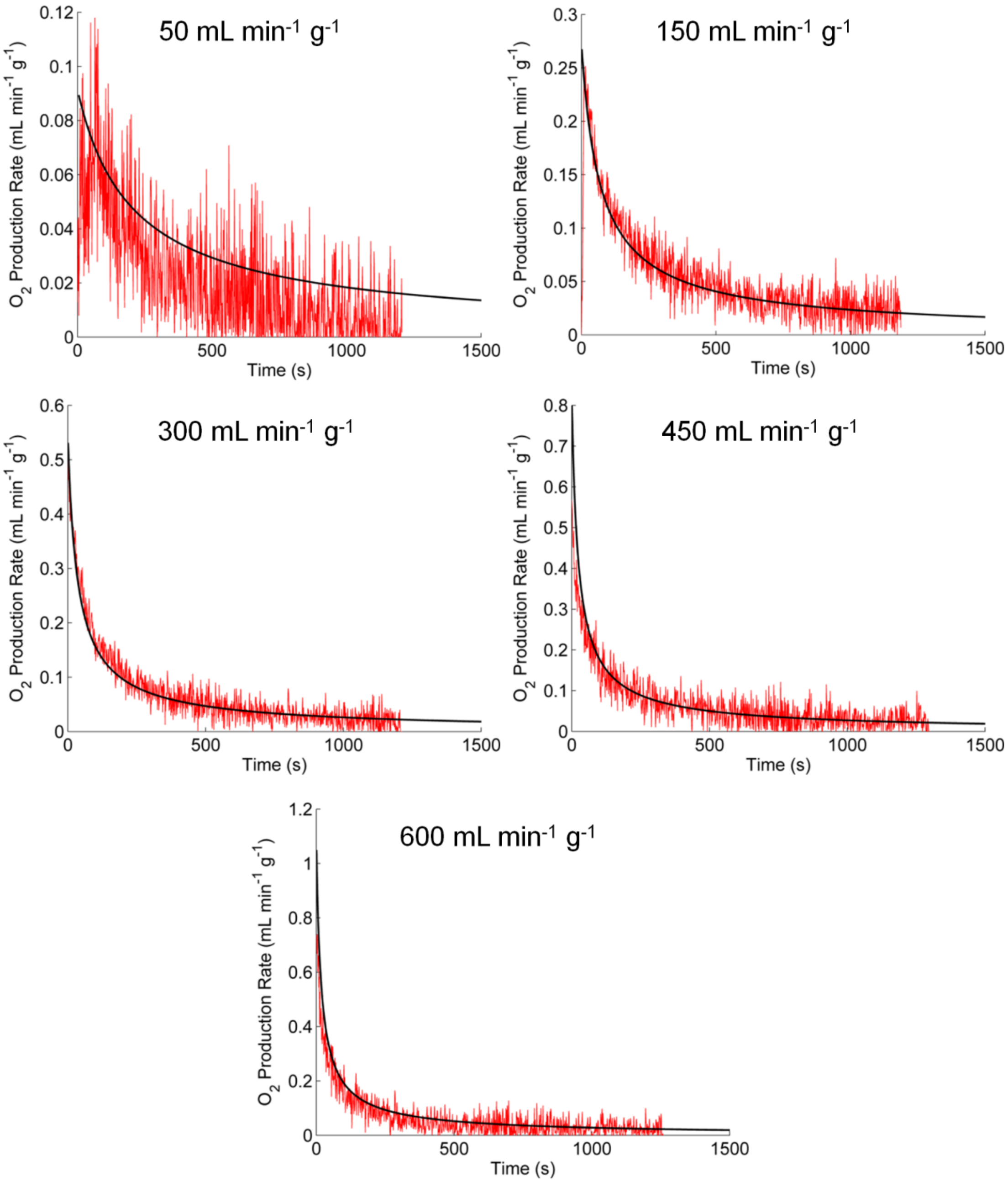

Figure 4.1 Quasi-equilibrium model (black) for isothermal reduction at 1500 °C compared to experimental data (red) over a range of sweep gas (p_{O_2} = 10^{-5} atm) flow rates.

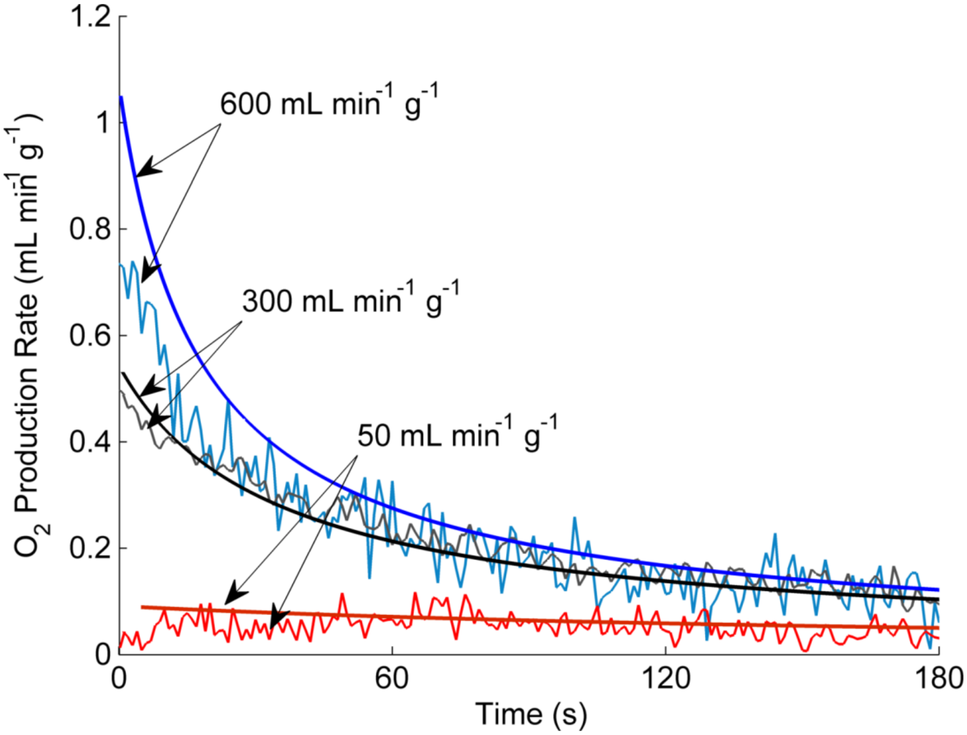

Figure 4.2 Comparison of quasi-equilibrium model and experimental data over the first 3 minutes of isothermal reduction at 1500 °C with sweep gas (p_{O_2} = 10^{-5} atm) flow rates of 50, 300, and 600 mL min^{-1} g^{-1}.

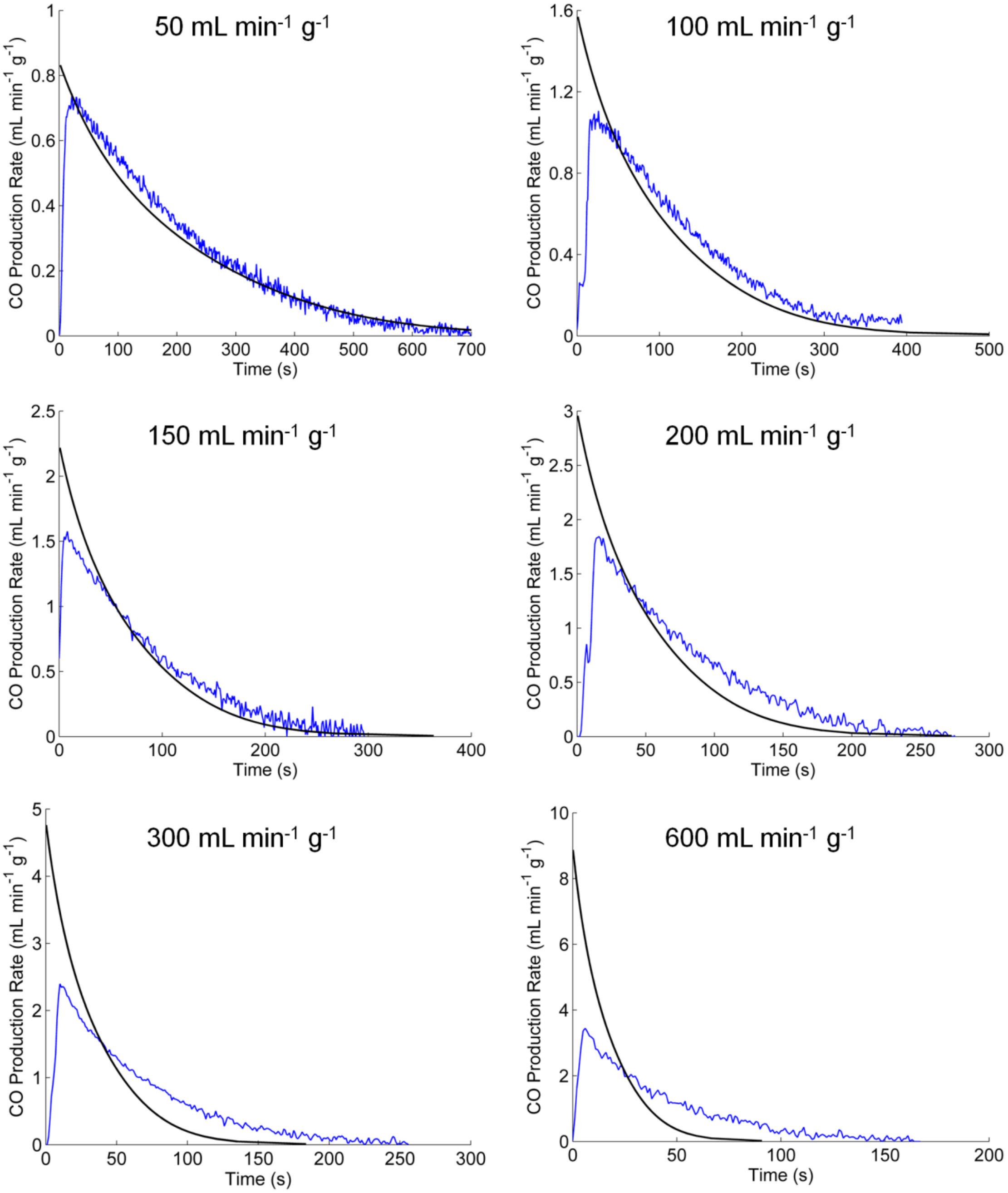

Figure 4.3 Quasi-equilibrium model (black) for isothermal oxidation with CO_2 at 1500 °C compared to experimental data (blue) over a range of CO_2 flow rates. For each flow rate, the initial δ for the model was selected to match the experimental data at that flow rate.

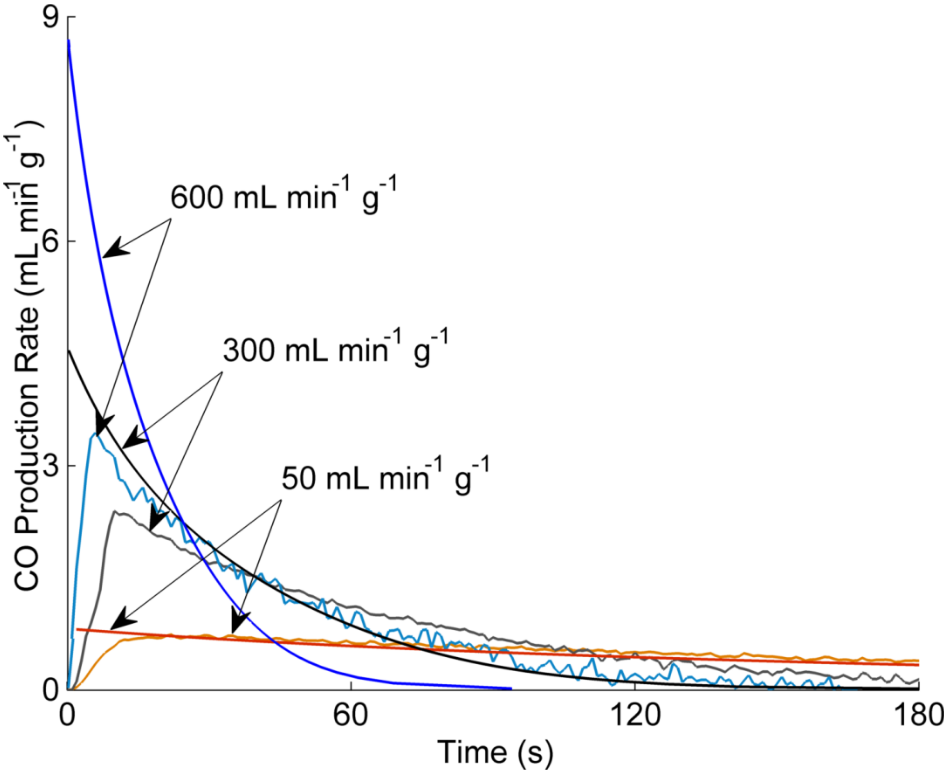

Figure 4.4 Comparison of quasi-equilibrium model and experimental data of isothermal oxidation at 1500 °C with CO_2 flow rates of 50, 300, and 600 mL min^{-1} g^{-1}.

Data for oxidation deviate from the quasi-equilibrium model to a greater extent and at lower flow rates than the data for reduction. This result may indicate that the surface reaction for oxidation is rate limiting at lower gas flow rates than the surface reaction for reduction[12]. Although measured oxidation rates deviate from the model at lower flow rates than for reduction, the close agreement at low flow rates (50–150 mL min^{-1} g^{-1}) suggests that quasi-equilibrium between the ceria and oxidizing gas limited the rates of oxidation at CO_2 flow rates below 150 mL min^{-1} g^{-1}.

---

[12] Another possibility, which has not yet been explored, is that as the flow rate increases, the CO_2 dissociation reaction is not rapid enough to satisfy the quasi-equilibrium condition.

4.3 Temperature Swing Quasi-equilibrium Model for Reduction

For ceria reduction taking place during a temperature swing, quasi-equilibrium can be maintained as long as the temperature ramp rate is slow enough that no other step in the reaction becomes the rate limiting step. In the limiting case of a step change in temperature, quasi-equilibrium would require a step change in δ and equation (4.4) would predict an infinite O_2 production rate. Thus, if the temperature is changed too rapidly, the quasi-equilibrium assumption is not valid. Furler *et al.* [17] present data (see Figure 7 in Ref. [17]) which suggest that ceria RPC in a prototype reactor remained in a state of quasi-equilibrium (calculated with a measured temperature and p_{O_2}) while reducing during a ramp from ~700–1600 °C with an average heating rate of 54 °C min^{-1} and a low mass specific sweep gas flow of 1.4 mL min^{-1} g^{-1} [13].

The possibility of quasi-equilibrium limiting reduction during a temperature ramp motivates the extension of the quasi-equilibrium model to non-isothermal conditions. However, since the temperature is no longer constant, the equilibrium p_{O_2} (and thus the O_2 production rate) is a function of both δ and temperature:

$$r_{O_2}(\delta, T(t)) = \frac{x_{O_2,out,red}(\delta, T(t)) \cdot \left(\dot{n}_{O_2,in} + \dot{n}_{N_2}\right) - \dot{n}_{O_2,in}}{1 - x_{O_2,out,red}(\delta, T(t))}. \tag{4.12}$$

Thus, equation (4.4) can no longer be separated and integrated to produce equation (4.5). Instead, a temperature profile is specified as a function of time and, starting from an

---

[13] The authors of Ref. [17], along with the authors of several other studies [10,11,15], conclude that the reduction of ceria during a temperature ramp is limited by heat transfer (i.e. the rate at which the ceria temperature can be changed). These observations are consistent with the idea that ceria remains in quasi-equilibrium with the sweep gas. If the ceria is in quasi-equilibrium during a temperature ramp reduction, the rate of reduction could be increased in two ways: increasing the temperature ramp rate (as observed by the references cited above) or increasing the sweep gas flow rate.

initial δ value, equation (4.12) yields the O_2 production rate at time $t = 0$. Then, stepping forward in time by a small amount Δt, the non-stoichiometry is updated using a discretized version of equation (4.4):

$$\delta(t + \Delta t) = \frac{r_{O_2}(\delta, T(t)) \cdot \Delta t}{K} + \delta(t). \tag{4.13}$$

Equations (4.12) and (4.13) are then solved at successive time steps until a desired modeling duration is reached. The solution procedure developed in Section 4.1 for isothermal operation is a special case of this more general solution procedure.

Figure 4.5 shows the reduction of porous ceria pellets during a temperature ramp (740–1480 °C) and under a sweep gas flow of 900 mL min^{-1} g^{-1}, compared to the results of the quasi-equilibrium model. The measured experimental temperature profile was used to generate the model's results.

Despite the relatively high sweep gas flow rate, the observed O_2 production rates in Figure 4.5 are very close to those predicted by the model. The O_2 production rate increases as the temperature rises. As soon as the temperature ramp ends, the O_2 production rate begins to decline. When the temperature begins to decrease at the end of reduction, the O_2 production rate quickly drops to nearly zero. In fact, in Figure 4.5, the quasi-equilibrium model predicts the O_2 production rate to drop below zero at t = 720 s, leveling off at -0.009 mL min^{-1} g^{-1}. This represents the slight oxidation of ceria with the 10 ppm O_2 impurity in the sweep gas. This reaction likely does take place, but due to the very low O_2 content in the sweep gas, it cannot be detected by the RLGA and its effect on the ceria's δ is negligible.

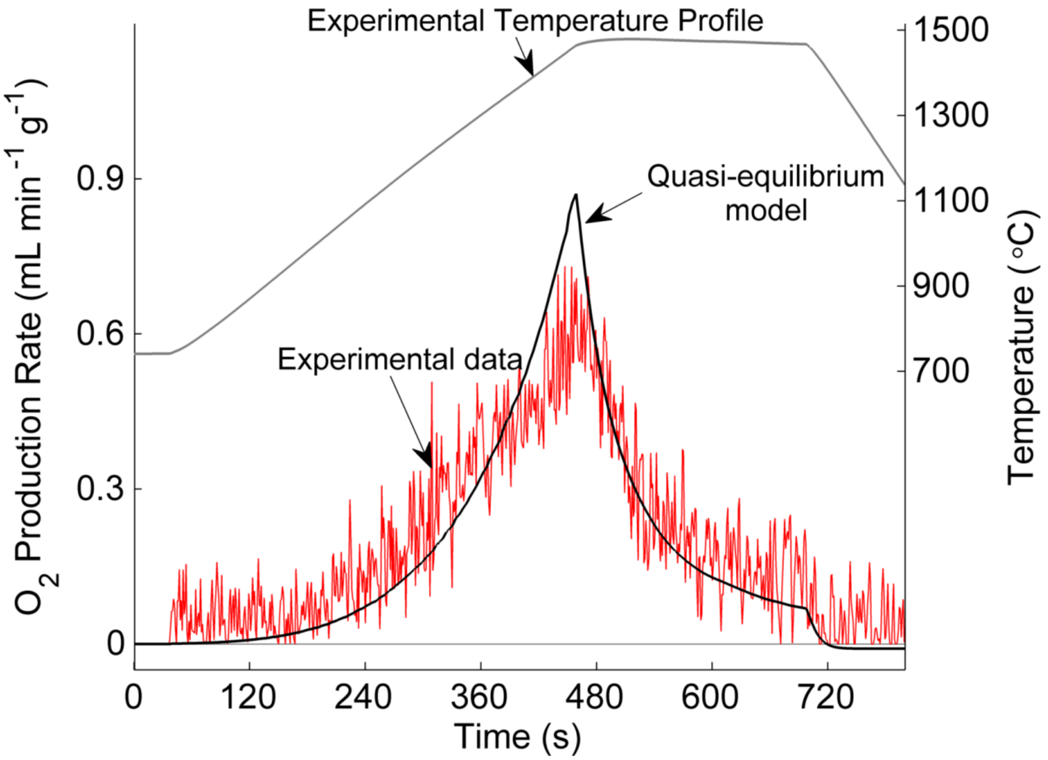

Figure 4.5 Comparison of temperature swing quasi-equilibrium model with temperature swing experimental data with porous ceria pellets under a sweep gas flow of 900 mL min^{-1} g^{-1}. The temperature ramp was from 740–1480 °C at 100 °C min^{-1}. Experimental temperature profile was used to generate the quasi-equilibrium model results.

4.4 Reaching the Thermodynamic Limit of Reduction with a Sweep Gas

When the efficiency of ceria redox cycles is analyzed in the literature, it is common practice to use the well-documented thermodynamics of ceria to predict the amount of fuel produced in a cycle [10,18–21,25,26], but little analysis has been put into assessing the reduction time required to reach equilibrium. The quasi-equilibrium model developed earlier in this chapter is now used to investigate this issue for isothermal reduction using a sweep gas.

As noted in Section 4.2, although the quasi-equilibrium model results in Figure 4.1 are only shown for 1500 s, the model predicts O_2 production to continue indefinitely while the O_2 production rate asymptotically approaches zero.

Now, consider the example case of isothermal reduction at 1500 °C with 150 mL min^{-1} g^{-1} sweep gas with an inlet p_{O_2} of 10^{-5} atm. Over the first 20 minutes of reduction, the model predicts a total O_2 production of 1.05 mL g^{-1}, very close to the experimentally measured value of 1.06 mL g^{-1}. However, the model predicts that in order to produce 90% of the thermodynamic limit of O_2 production for these conditions (2.54 mL g^{-1}), a reduction time of nearly 10 hours is required. The reason for this very long reduction time is that as the non-stoichiometry approaches reduction equilibrium, the p_{O_2} of the sweep gas exiting the ceria pellet bed approaches the p_{O_2} of the sweep gas at the inlet of the bed (10^{-5} atm in the example case), decreasing the amount of O_2 that the sweep gas can carry away from the ceria. The rate at which the sweep gas carries away O_2 becomes so slow that it takes a long time (and a large quantity of sweep gas) to appreciably change the ceria's non-stoichiometry.

Figure 4.6 shows the fraction of the thermodynamic O_2 production for isothermal reduction at 1500 °C with 150 mL min^{-1} g^{-1} of sweep gas as a function of time. To reach 90+% of the thermodynamic limit of O_2 production under these conditions with sweep gas of p_{O_2} = 10^{-4}, 10^{-5}, and 10^{-6} atm requires reduction times on the order of 1, 10, and 100 hours, respectively[14].

---

[14] The thermodynamic limit of O_2 production increases significantly with lower sweep gas p_{O_2}, so the O_2 production *rates* will increase slightly with lower p_{O_2} despite the fact that it takes longer to approach equilibrium.

These results suggest that it would be very inefficient to reach reduction equilibrium using a high-purity sweep gas because it would take a prohibitively long time and would use (and need to heat up) an enormous amount of sweep gas. This conclusion agrees with the results of my cycle period optimization (see Chapter 3), which found short cycles to be more efficient than long ones. These results caution against using ceria thermodynamics to predict the fuel production of ceria redox cycles, especially when low sweep gas p_{O_2} is assumed, since reaching equilibrium would require an unreasonably long period of time.

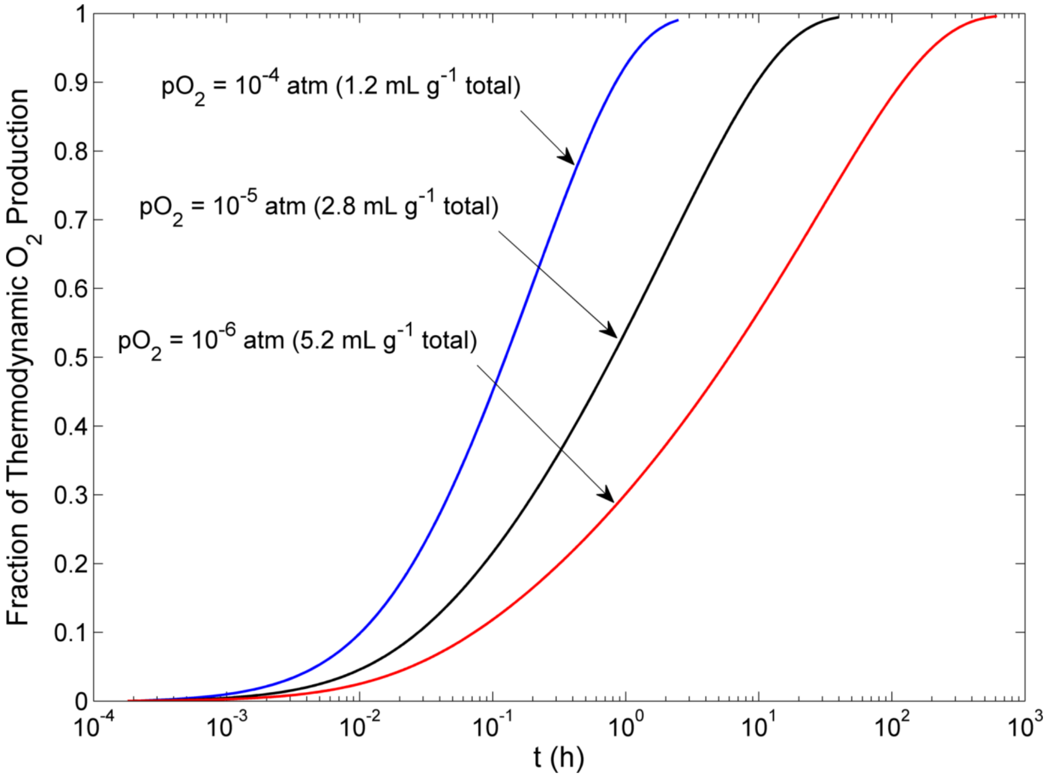

Figure 4.6 Fraction of thermodynamic O_2 production as a function of time, predicted by the quasi-equilibrium model for isothermal reduction at 1500 °C with a sweep gas flow rate of 150 mL min^{-1} g^{-1} and for sweep gas p_{O_2} = 10^{-4}, 10^{-5}, and 10^{-6} atm.

4.5 Efficient Utilization of Sweep Gas

Due to the energy penalties of producing sweep gas and heating it to the reactor temperature, it is important, from a cycle efficiency standpoint, to use sweep gas efficiently (i.e., to use as little sweep gas as possible to carry away a fixed amount of O_2).

While my efficiency analysis of isothermal ceria cycling (see Chapter 3) used gas flow rates based on experimental data, most thermodynamic analyses in the literature use a model to calculate the required sweep gas flow. One model [18–20] assumes that the sweep gas and the produced O_2 are perfectly mixed so that a uniform p_{O_2} is maintained, at which the sweep gas leaves the reactor.

Bader *et. al.* [20] present an argument for a counterflow of ceria and sweep gas (explained as ceria physically moving in the opposite direction as the sweep gas flow), which yields the most efficient possible utilization of sweep gas (i.e. requires the least amount of sweep gas for a given amount of O_2 production). Although the physical explanations behind the "perfectly mixed" and "counterflow" models differ, both use the same general equation to calculate the sweep gas requirement:

$$\dot{n}_{N_2} = \dot{n}_{O_2}\left(\frac{p_{O_2,out}}{p_{tot} - p_{O_2,out}} - \frac{p_{O_2,in}}{p_{tot} - p_{O_2,in}}\right)^{-1}, \qquad (4.14)$$

where $\dot{n}_{N_2}$ is the flow rate of N_2, $\dot{n}_{O_2}$ is the O_2 production rate, p_{tot} is the total pressure of the reactor, $p_{O_2,in}$ is the O_2 partial pressure of the sweep gas entering the reactor, and $p_{O_2,out}$ is the O_2 partial pressure of the sweep gas leaving the reactor. The second term in the parentheses in equation (4.14) is typically small compared to the first, and is often neglected (e.g., in Refs. [18,19] and in the perfectly mixed model in Ref. [20]).

Mathematically, the perfectly mixed and counterflow models are identical; they differ only in the choice of $p_{O_2,out}$ and the physical descriptions used to justify that choice.

In the mixed flow model, a desired $p_{O_2,out}$ is specified. Different assumptions for the value of $p_{O_2,out}$ lead to drastic differences in the predicted sweep gas requirement. In the counterflow model, the O_2 partial pressure of sweep gas *leaving* the reduction zone of a continuous-operation reactor ($p_{O_2,out}$) is fixed to the equilibrium p_{O_2} of the ceria *entering* the reduction zone. For isothermal operation, $p_{O_2,out}$ corresponds to the equilibrium state of ceria under the oxidizer flow and at the reactor temperature—this is the maximum possible p_{O_2} that can be achieved by the sweep gas in isothermal cycling, and thus is the most efficient utilization of sweep gas to remove O_2 from the ceria.

The quasi-equilibrium model discussed in this chapter is very similar to the counterflow model because it uses the thermodynamics of ceria to limit the amount of O_2 that is carried away by the sweep gas. The only difference is that the counterflow model assumes a continuous-operation reactor in which ceria constantly moves between reduction and oxidation zones, while the quasi-equilibrium model applies to the transient reduction of stationary ceria. At the very beginning of transient reduction, when the ceria is at the oxidation equilibrium non-stoichiometry, the quasi-equilibrium model is equivalent to the counterflow model. Stated another way, the counterflow model uses an argument of "flowing" ceria to allow the peak performance of the quasi-equilibrium model to be sustained indefinitely.

The fact that experimental data over certain gas flow rates (≤ 300 mL min^{-1} g^{-1} for isothermal reduction, ≤ 150 mL min^{-1} g^{-1} for isothermal oxidation, higher flow rates for reduction during a temperature ramp) agree with the quasi-equilibrium model (see Figures 4.1, 4.2, and 4.5) means that for these cycling conditions, sweep gas is being used as efficiently as possible for the transient reduction of stationary ceria. Improving the efficiency of sweep gas utilization is only possible by changing the assumptions of the model or changing the cycle operation in a manner not accounted for in the model presented here. Possible avenues for improving the efficiency of sweep gas usage include changing the reactive material (to alter the underlying thermodynamics), introducing a temperature swing (or modifying the existing temperature swing)[15], lowering the total pressure of the reactor using a vacuum pump, or possibly by alternating the direction of sweep gas and CO_2 flows through the ceria pellet bed to establish gradients in the ceria non-stoichiometry (which are ignored in the model presented above) that approximate the physical configuration of counterflowing ceria and sweep gas.

---

[15] Beginning reduction at a lower temperature and non-stoichiometry as compared to isothermal cycling (and assuming a reasonable temperature ramping rate), ending reduction at a higher temperature, and increasing the temperature ramping rate all allow for higher equilibrium p_{O_2} values, which correspond to more efficient sweep gas usage.

5 Wood Templated Ceria

This chapter reports the experimental testing of wood templated ceria, a new morphology for thermochemical fuel production. This work was completed in collaboration with Camille Malonzo and Dr. Andreas Stein from the University of Minnesota Department of Chemistry, who developed, synthesized, and characterized the wood templated ceria. I tested the wood templated ceria in an infrared imaging furnace at reduction temperatures from 1200–1500 °C and a fixed oxidation temperature of 800 °C to investigate the cycling performance and the sintering resistance of the wood templated ceria. The reduction and oxidation performance of wood templated ceria were analyzed and compared with nonporous ceria powder.

5.1 Review of Prior Work

There is an expanding interest in developing new material architectures for metal oxides used in solar thermochemical cycles to split water or carbon dioxide [10,11,13,14,16,17]. The overall consensus of prior work is that it is desirable to develop material structures that permit optimal solar penetration and absorption, rapid heat transfer, minimal pressure drop, high reactivity, and long term stability for cycling at temperatures as high as 1500 °C. High surface area is particularly crucial for oxidation, in which the heterogeneous surface reaction has been found to be the rate limiting step [10,13,17].

In one of the earliest efforts to produce high specific surface area (SSA) ceria structures, Chueh *et al.* [10] synthesized a porous ceria monolith with a SSA of 0.1 m^2 g^{-1} and a porosity of ~70% using a fugitive pore former. After heat treating the monolith at 1500 °C for three hours to stabilize its microstructure, it was used to demonstrate water splitting over 500 cycles in which the material was reduced at 1500 °C and oxidized with steam at 800 °C. Steady oxidation rates (averaged over the time required to produce 90% of the H_2) of 1.3 mL min^{-1} g^{-1} were demonstrated after a decline from 3.2 mL min^{-1} g^{-1} over the first 100 cycles. The initial decrease in H_2 production rates was attributed to a loss in surface area caused by sintering, although the SSA of the monolith after cycling was not reported [10]. Hao *et al.* [21] synthesized ~80% porous ceria monoliths by wetting ceria powder with isopropanol, pressing it into a mold, and sintering at 1500 °C for two hours. These monoliths were cycled isothermally at 1500 °C, and displayed signs of a changing microstructure over 22 cycles (seven hours). The same procedure used by Hao *et al.* [21] was also used to produce 65% porous monoliths which were heat treated at 1500 °C for six hours; the rates of CO production in an isothermal CO_2 splitting cycle were steady over 102 cycles, indicating a stable microstructure [2].

ETH-Zurich has compared a number of ceria structures, including the porous monoliths developed by Chueh et al. [15], commercial ceria felt made of μm-scale fibers [16,17], and reticulated porous ceramic (RPC) [17,27] in a prototype solar reactor. Maximum measured reduction temperatures varied from 1500 °C to 1640 °C, depending on the power input to the reactor. The porous monoliths exhibited high mass-specific oxidation rates (peak rates of 3.0–4.6 mL min^{-1} g^{-1} for CO_2 splitting) [15]. Ceria felt and a ceria RPC were compared under the same radiative power inputs and total gas flow rates, albeit with vastly different amounts of ceria mass (1413 g with RPC, 90 g with felt). The felt had a much higher SSA than the RPC (6.0 m^2 g^{-1} compared to 1.45×10^{-4} m^2 g^{-1}) and displayed peak CO production rates nine times that of the RPC on a unit mass basis (reduction was not limited by the surface reaction, so O_2 production rates were similar on a unit mass basis) [17]. However, SEM images of the felt provided strong evidence of sintering after 10 cycles [16], while the RPC demonstrated excellent sintering resistance, with no deterioration of the microstructure after 14 cycles [17]. Because the reactor used for the comparison could hold 15.7 times more ceria mass when loaded with RPC than with felt, the reactor efficiency was higher with the RPC (1.73% vs. 0.15%) [17]. However, this result is an artifact of the reactor design, which limited the volume available for the ceria structures. A number of papers point out the potential benefits of RPCs for volumetric absorption of radiation [34–37]. Recently, Furler *et al.* [27] improved the SSA of an RPC structure by implementing dual-scale porosity by fabricating the struts of the RPC with μm-scale porosity. The mm-scale pores of the RPC structure provide favorable radiative heat transfer properties, while the μm-scale pores in the struts increase the SSA to promote rapid heterogeneous reactions. Compared in a prototype solar reactor to a conventional RPC (SSA = 1.45×10^{-4} m^2 g^{-1}), the dual-porosity RPC (SSA = 0.066 m^2 g^{-1}) decreased the time required for oxidation by a factor of three [27].

Gibbons *et al.* [12] used an electrospinning process to create μm-scale fibers of 2.5% Zr-doped ceria that maintained relatively high SSA up to 1400 °C. The fibers were thermochemically cycled in an infrared imaging furnace at a reduction temperature of 1400 °C, a temperature which was, for the electrospun fibers, a compromise between the thermodynamic benefits of high reduction temperature and the problem of sintering at elevated temperature. After the first ~60 cycles (~17 hours), steady cycling was observed over ~45 cycles (~13 hours) with peak CO production rates of 14 mL min^{-1} g^{-1}. The surface area of the fibers stabilized at 0.3 m^2 g^{-1} [12].

Templated macroporous structures such as three-dimensionally ordered macroporous (3DOM) ceria structures offer the potential for high SSA, but sintering is significant above 1200 °C [11,13,14]. Rudisill *et al.* [11] cycled 3DOM ceria at a reduction temperature of 1250 °C followed by oxidation at 875 °C. The low reduction temperature permitted the 3DOM to retain a high SSA (4 m^2 g^{-1} after 50+ cycles), allowing fast oxidation rates and an average fuel production rate of 0.8 mL min^{-1} g^{-1} [11]. The rate of production of CO was an order of magnitude higher than for a nonporous ceria powder subjected to the same cycling conditions [11].

In the present work, a new templated ceria morphology is explored for thermochemical redox cycling: wood templated (WT) ceria. As the name suggests, wood templated ceria replicates the microstructure of wood, which has a porous structure consisting of a series of channels on the order of tens of microns in diameter. It is hypothesized that this structure provides a balance between sufficient SSA for rapid heterogeneous reactions and solid features large enough to resist sintering at temperatures useful for ceria reduction. The WT ceria is thermochemically cycled in an infrared imaging furnace at reduction temperatures of 1200–1500 °C to investigate how well the

WT ceria resists sintering. The WT ceria is also compared with a nonporous ceria powder at reduction temperatures of 1400 °C and 1500 °C. Oxidation rate data are plotted as a functions of ceria non-stoichiometry in order to fairly compare oxidations which begin at different non-stoichiometries.

5.2 Morphologies

5.2.1 Wood Templated Ceria

Softwoods such as *P. strobus* (eastern white pine), the wood used to template ceria in this work, have a porous microstructure made up of channels 20 to 50 μm in diameter [38]. This structure, replicated with ceria, provides internal surface area to enhance the rates of heterogeneous reactions.

All WT ceria samples were synthesized by Camille Malonzo[16]. Centimeter-sized pieces of wood were soaked in a liquid ceria precursor. After the precursor infiltrated the wood and coated its surface, the wood was heated in an oven to remove the wood, leaving only ceria, which was crushed into a powder. The ceria replicated the pore structure of the wood, but with thinner walls (0.5–1 μm for the WT ceria, compared to 1–10 μm for the wood) [38]. The μm-scale solid features of the WT ceria are larger than the 100 nm-scale features of 3DOM ceria, another templated structure [11,13,14]. These larger solid features are expected to improve the sintering resistance of the WT ceria at the high temperatures useful for ceria reduction.

---

[16] University of Minnesota Department of Chemistry. Dr. Andreas Stein, advisor.

To sinter and stabilize the microstructure so that subsequent thermochemical cycling would be steady and would be indicative of the material's long-term performance, each WT ceria sample was held at its target reduction temperature for four hours in a Carbolite STF 16/180 tube furnace under an atmosphere of static air. Figure 5.1 shows an SEM image of WT ceria after heat treatment at 1400 °C (image courtesy of Camille Malonzo). It retains the porous microstructure of the wood from which it was templated. After this heat treatment, the WT ceria samples were sieved from 180–850 μm.

Table 5.1 reports the surface area of WT ceria after heat treatment at each reduction temperature (surface area measurements from Camille Malonzo). As anticipated, the surface area decreases at the higher temperatures as the result of sintering.

Table 5.1 BET surface area (based on krypton sorption) of heat treated ceria samples and the slopes of curves plotted in Fig. 5.8. Surface area measurements were performed by Camille Malonzo (University of Minnesota, Dept. of Chemistry).

Morphology	Heat Treatment Temperature (°C)	BET SSA (m^2 g^{-1})	Slope of $\dot{V}'_{CO}$ vs. δ in Fig. 5.8 (mL mol_{CeO2} min^{-1} g^{-1} mol_{vac}^{-1})
WT	1200	0.22	1300
WT	1300	0.23	800
WT	1400	0.10	800
WT	1500	<0.05[a]	70
Nonporous	1400	<0.05[a]	70
Nonporous	1500	<0.05[a]	30

[a] 0.05 m^2 g^{-1} is the minimum SSA that can be accurately measured using krypton sorption

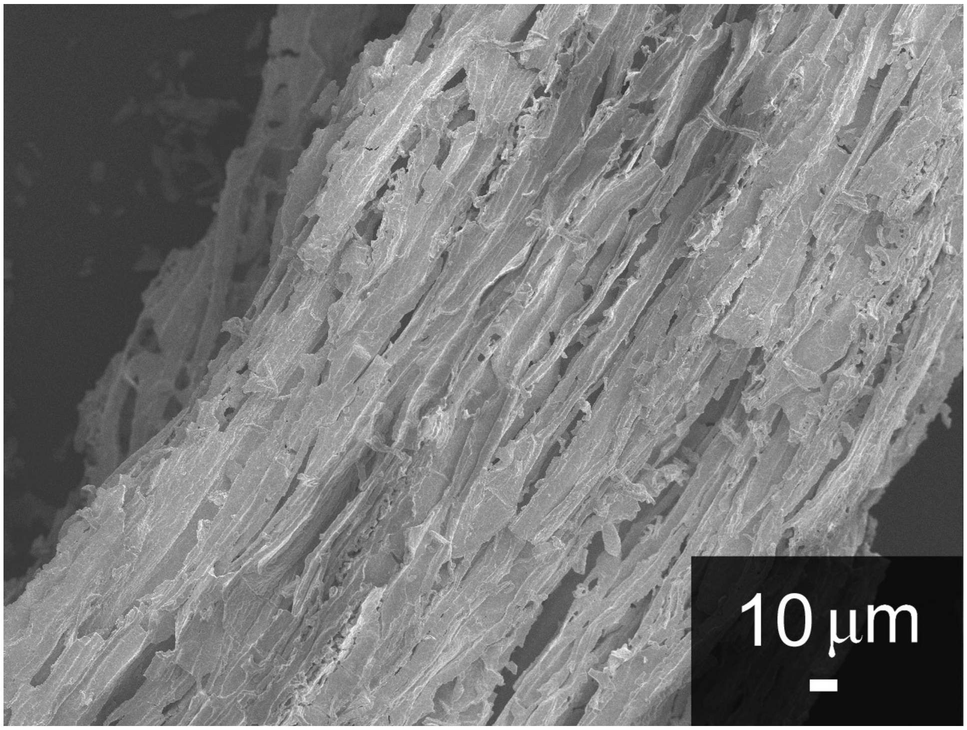

Figure 5.1 Scanning electron microscope image of WT ceria after heat treatment at 1400 °C for 4 hours. The ceria still retains the microstructure of the wood it was templated with. Image courtesy of Camille Malonzo.

5.2.2 Nonporous Ceria

The cycling behavior of the WT ceria is compared to that of a nonporous ceria powder. The powder was made by crushing 3–6 mm nonporous particles of ceria (Alfa Aesar, 99.9% pure) with a mortar and pestle and then sieving the pieces from 180–850 μm to give the same range of particle sizes as the WT ceria. As with the WT ceria, each nonporous ceria sample was heat treated for four hours at the target reduction temperature in an atmosphere of static air.

Figure 5.2 shows an SEM image of the nonporous ceria powder (image courtesy of Camille Malonzo). There is no visual evidence of internal porosity. The measured SSA of all nonporous ceria samples were below 0.05 m^2 g^{-1}, the detectable limit for krypton sorption (see Table 5.1).

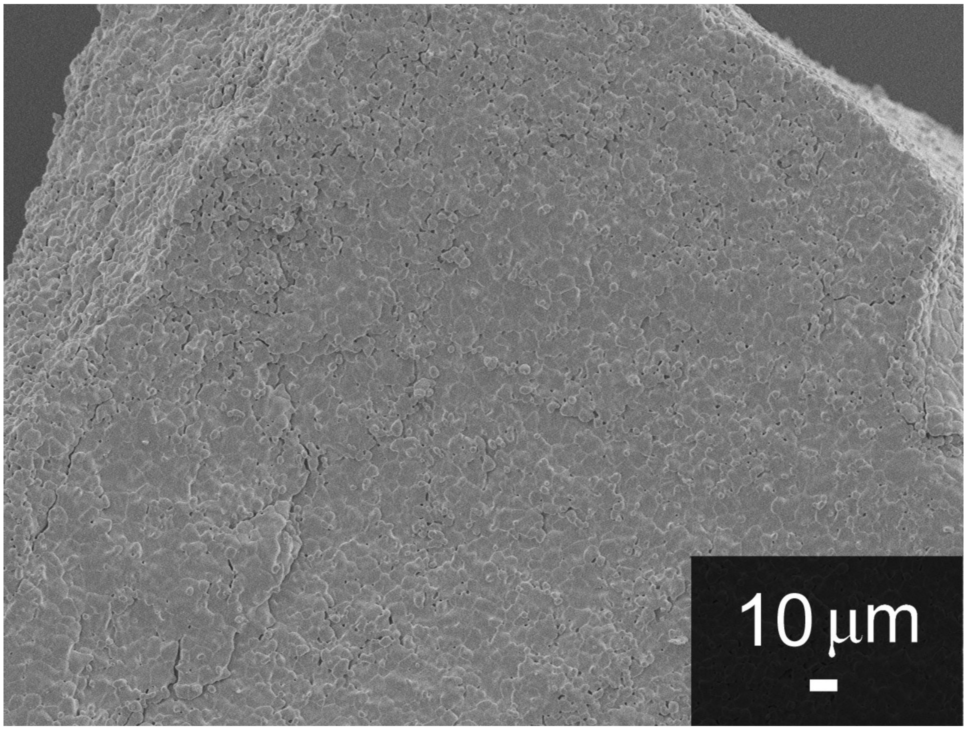

Figure 5.2 Scanning electron microscope image of nonporous ceria after heat treatment at 1400 °C for 4 hours. The ceria powder has no appreciable porosity. Image courtesy of Camille Malonzo.

5.3 Experimental Methodology

5.3.1 Apparatus and Procedure

Wood templated and nonporous ceria powders were thermochemically cycled in an infrared imaging furnace. Figure 5.3 shows a sketch of the experimental setup. Ceria (0.5 g) was loosely loaded into a 9.5 mm i.d. alumina tube, forming a bed of powder 4–10 mm long, which was held in place with a porous alumina disk. The alumina tube was placed horizontally in the infrared imaging furnace (ULVAC RIKO VHT-E44), and a Pt/Pt-Rh thermocouple was inserted in each side of the tube. The thermocouple positioned downstream of the bed was used to control the power of the furnace, and the second thermocouple was embedded in the ceria sample to monitor its temperature. Sweep and oxidizing gas flows were regulated with mass flow controllers (with an accuracy of ± 1% of the flow) and a series of pneumatic valves. The product gas stream exiting the furnace was monitored for O_2 and CO using a Raman Laser Gas Analyzer (RLGA) with a sampling frequency of 1 Hz and an accuracy of ±0.02 mol%.

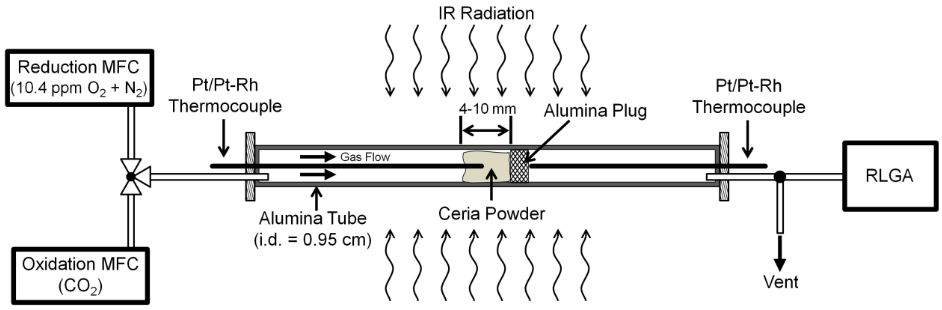

Figure 5.3 Experimental apparatus (not to scale), comprising a ceria sample in an alumina tube, a gas flow control system, and gas analysis equipment. The ceria sample is exposed to concentrated IR radiation in an IR imaging furnace.

Wood templated ceria was tested at reduction temperatures from 1200–1500 °C in 100 °C increments with a fixed oxidation temperature of 800 °C to investigate the rates of reduction and oxidation as well as the sintering resistance of the WT morphology. Nonporous ceria powder was cycled at reduction temperatures of 1400 °C and 1500 °C for comparison with the WT ceria. Each experiment consisted of 21 cycles. During thermochemical cycling, heat treated ceria was first reduced under a 250 mL min^{-1} flow of inert sweeping gas (10 ppm O_2 in N_2) by ramping the temperature from 800 °C to the target reduction temperature at a rate of 200 °C min^{-1} [17]. The reduction temperature was held for 5 minutes. Although this time was insufficient for the reduction reaction to reach equilibrium, the longer reduction periods required to approach equilibrium would require large quantities of sweep gas and would yield low average rates of reduction. After reduction, the temperature was lowered to 800 °C at a rate of 200 °C min^{-1} and oxidation was initiated by flowing 250 mL min^{-1} of CO_2 (99.99% purity) over the bed. Oxidation conditions proceeded until oxidation reached completion.

---

[17] While the IR furnace has the capability to change temperature very rapidly, relatively slow temperature ramp rates of 200 °C min^{-1} were chosen to limit the temperature overshoot caused by the time response of the thermocouple used to control the furnace. The Pt/Pt-Rh thermocouples used for furnace control were measured to have 1st order time constants of 10-20 s over the range of temperatures experienced in redox cycling.

5.3.2 Data Analysis

The transient rates of O_2 and CO production were calculated as

$$\dot{V}_i' = \frac{x_i \dot{V}_{total}}{m_{CeO_2}}, \tag{5.1}$$

where $\dot{V}_i'$ is the volumetric rate of O_2 or CO production per unit mass of ceria (evaluated at the reference conditions of 25 °C, 1 bar); x_i is the mole fraction of O_2 or CO in the product stream, measured by the RLGA; $\dot{V}_{total}$ is the total volumetric flow rate (also evaluated at the reference conditions); and m_{CeO_2} is the mass of the ceria sample.

Oxidation rates of the WT and nonporous ceria are compared at the same values of δ. This approach, as compared to the approach used in prior studies [11,13,14,17,21] of comparing rates versus oxidation time, provides an assessment of the effects of reduction temperature and material morphology on the rate of oxidation for situations in which oxidation is initiated at different non-stoichiometries. The ceria non-stoichiometry during oxidation, δ, was evaluated using the CO production rate data:

$$\delta(t) - \delta_{eq} = \frac{M_{\mathrm{CeO_2}} P_{ref}}{R T_{ref}} \int_{t}^{t_{\mathrm{eq}}} \dot{V}_i'(\hat{t}) d\hat{t}\,, \tag{5.2}$$

where $M_{\mathrm{CeO_2}}$ is the molecular weight of ceria, P_{ref} and T_{ref} are the reference pressure (1 bar) and absolute temperature (298.15 K), t_{eq} is the time the ceria reaches equilibrium at the end of oxidation, and δ_{eq} is the equilibrium non-stoichiometry at t_{eq} ($\delta_{\mathrm{eq}} \cong 0$ for oxidation at 800 °C with CO_2).

5.4 Results

Figure 5.4 shows a representative cycle for WT ceria at a reduction temperature of 1400 °C. As the temperature of the ceria was ramped from 800 °C to 1400 °C under the sweep gas flow, O_2 was produced, reaching a peak rate of 0.6 mL min^{-1} g^{-1} at 1400 °C. During the five minute dwell at 1400 °C, the O_2 production rate fell below the detection limit of the RLGA (0.01 mol%). Despite the decline to extremely slow O_2 production rates, the reduction reaction did not reach equilibrium: a total of 0.8 mL g^{-1} of O_2 was produced, while equilibrium thermodynamics predicts a total of 2.1 mL g^{-1} at 1400 °C with a sweep gas of 10 ppm O_2 [9]. After the five minute dwell at 1400 °C, the temperature was lowered to 800 °C and the gas flow was switched to CO_2. Carbon monoxide was produced immediately, quickly reaching a peak rate of 9 mL min^{-1} g^{-1} and then decaying as the oxygen vacancies created during reduction were filled.

Cycling behavior of the heat treated materials was steady over 21 reduction/oxidation cycles for all tests, displaying no evidence of further material sintering. Figure 5.5 shows cyclic rates of O_2 release and CO production for WT ceria at a reduction temperature of 1400 °C. The slight decline in peak CO production rates over the final eight cycles is due to a decrease in peak reduction temperature from 1410 °C to 1400 °C. This variation in temperature is attributed solely to control of the furnace. All cycles for each reduction temperature and morphology are reported in Appendix B.

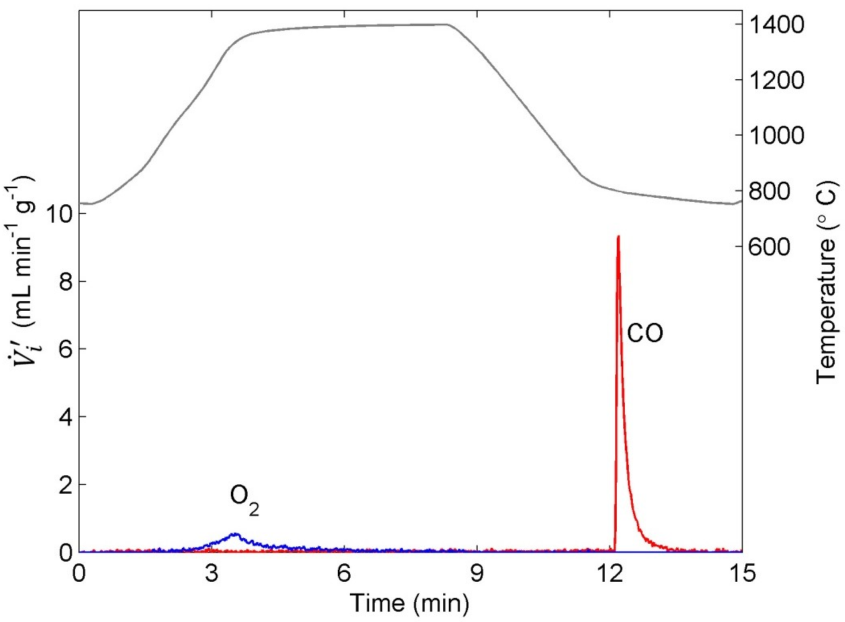

Figure 5.4 Temperature, O_2 production rate, and CO production rate from cycle #14 of the WT ceria test with reduction at 1400 °C and oxidation at 800 °C.

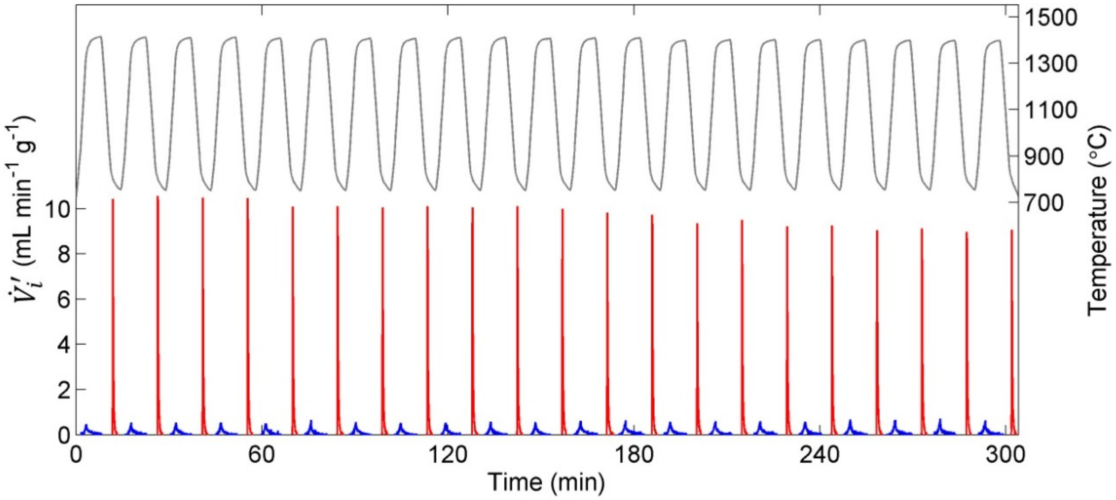

Figure 5.5 Cycling data for WT ceria at a reduction temperature of 1400 °C. CO (red) and O_2 (blue) production rates and the temperature measurement from the thermocouple embedded in the ceria sample (gray) are shown over 21 cycles. The decline in peak CO production rates was caused by a decrease in peak reduction temperatures from 1410 °C to 1400 °C.

Figure 5.6 compares O_2 production rates during a typical reduction from each experiment. For the WT ceria, peak O_2 production rates increased with increasing reduction temperature, as expected from chemical thermodynamics [9]. The rate of reduction followed the temperature ramps, consistent with other studies [10–12]. The O_2 production rates of the nonporous ceria are noticeably lower than those of the WT ceria samples when reduced under the same conditions. This result suggests that the very low SSA of the nonporous ceria caused reduction to be limited by the surface reaction.

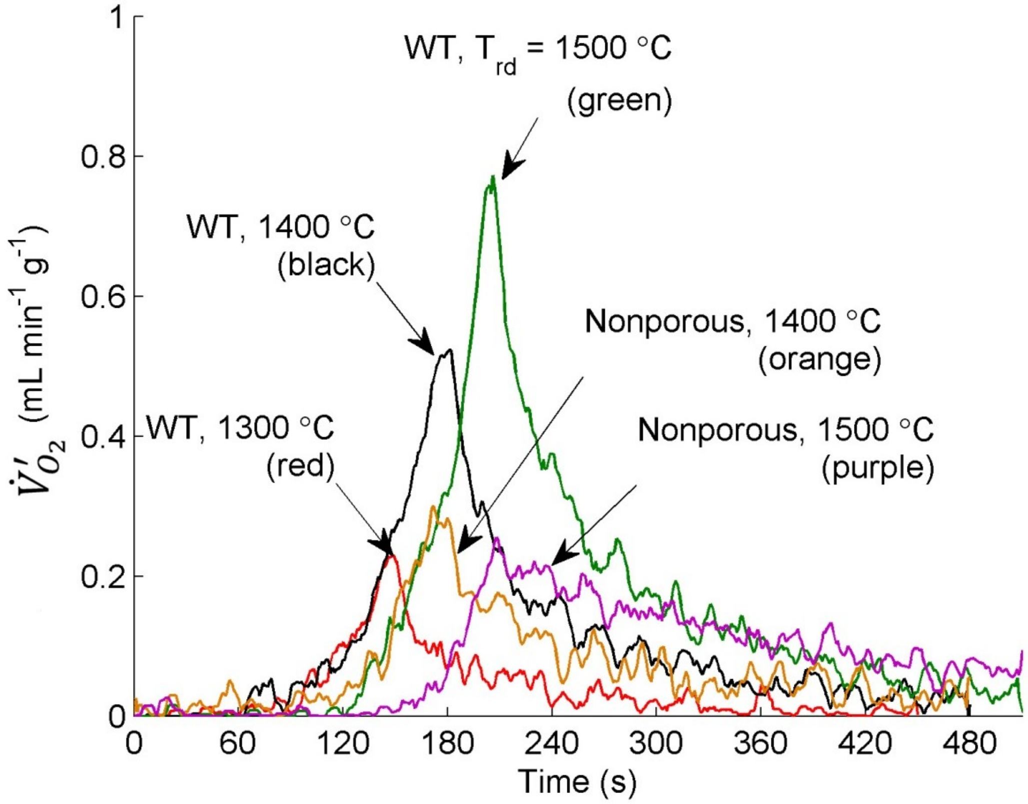

Figure 5.6 O_2 production rates of a typical cycle from each experiment. The WT ceria test at a reduction temperature of 1200 °C did not produce O_2 at rates measureable by the RLGA.

Representative oxidations at 800 °C following reductions at 1200−1500 °C for WT ceria and at 1400–1500 °C for nonporous ceria are compared in Figure 5.7. For WT ceria, the peak CO production rate increased as the reduction temperature was raised from 1200 °C to 1400 °C, consistent with the improved reduction thermodynamics. However, after reduction at 1500 °C, the CO production rates decreased by a factor of seven compared to oxidation after reduction at 1400 °C, from 9 mL min^{-1} g^{-1} to 1.3 mL min^{-1} g^{-1}. The decreased CO production rates following reduction at 1500 °C corroborate

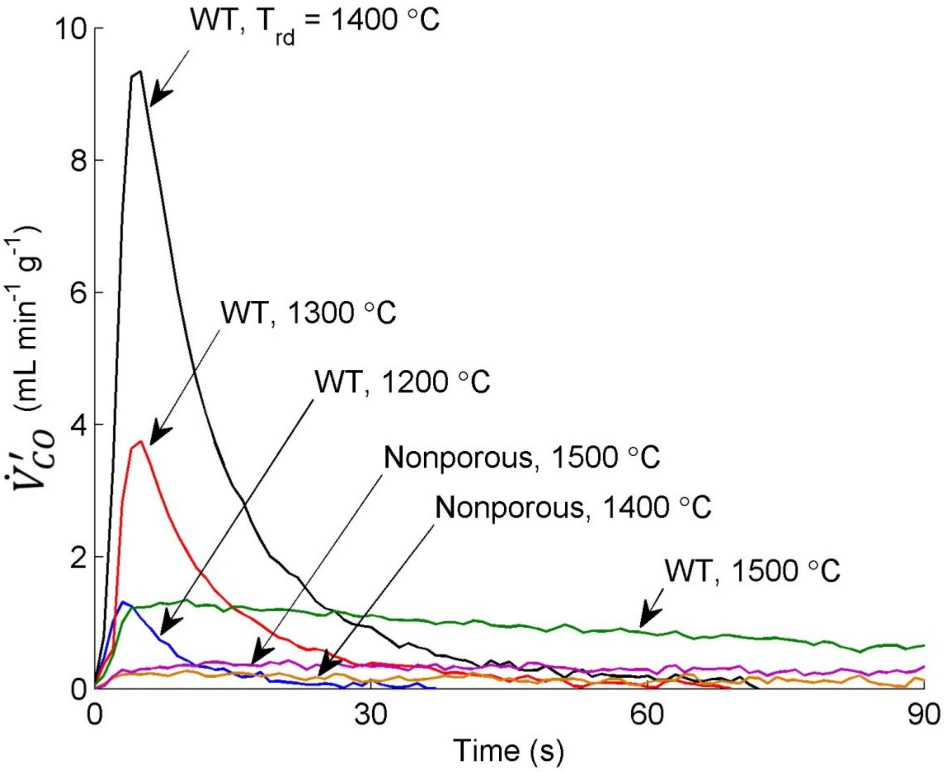

Figure 5.7 CO production rate in time for WT ceria at 800 °C following reduction at temperatures ranging from 1200–1500 °C, and for nonporous ceria powder at 800 °C following reduction at 1400–1500 °C. The WT sample reduced at 1500 °C and both of the nonporous ceria samples continue to produce CO after 90 s (not shown).

the decline in SSA from 0.1 m^2 g^{-1} after heat treatment at 1400 °C to <0.05 m^2 g^{-1} after heat treatment at 1500 °C (Table 5.1). The peak CO production rates for all WT ceria samples were higher than those of the nonporous ceria samples, which had specific surface areas of <0.05 m^2 g^{-1}.

Oxidation rates of the two morphologies over the range of reduction temperatures evaluated are plotted versus ceria non-stoichiometry in Figure 5.8 [18]. This figure reinforces the advantages of the WT material. The rate data are plotted from the non-stoichiometry reached at the end of every oxidation (δ = 0) to the maximum non-stoichiometry attained during the preceding reduction. The maximum δ depended on the morphology and the reduction temperature; for both morphologies, the maximum δ increased monotonically with reduction temperature. Moreover, at a fixed morphology and reduction temperature, the rate of oxidation increased with increasing non-stoichiometry. This effect was expected because a higher δ signifies a higher concentration of oxygen vacancies in the ceria, which participate in the oxidation reaction. The dependency of oxidation rate on δ is supported by kinetic models of ceria oxidation [32,39]. The benefits of the wood templating are significant. At each reduction temperature, the WT ceria reached a higher non-stoichiometry than the nonporous ceria. Furthermore, the WT ceria produced CO faster at each δ. The rate of oxidation for the WT material is 5–6 times faster than the nonporous ceria after reduction at 1400 °C and 2–3 times faster after reduction at 1500 °C.

---

[18] The rate data prior to the peak rates in Figure 5.7 were excluded from Figure 5.8 because they were influenced by the changing gas flow conditions between reduction and oxidation and therefore did not accurately represent the oxidation rates at the δ values calculated for them with equation (5.2).

The detrimental effect of reduced SSA on the rate of oxidation is reflected by the differences in the slope of the curves in Figure 5.8 (quantified in Table 5.1). The rate of increase of oxidation rate with non-stoichiometry is slowest for the non porous material, for which the SSA is <0.05 m^2 g^{-1}, regardless of reduction temperature. For the WT material, from 1200 °C to 1400 °C, small reductions in the slope are consistent with only modest changes in SSA with increasing reduction temperature. Thus, for WT ceria, the benefit of improved reduction thermodynamics from 1200 °C to 1400 °C outweighed the detrimental effect of sintering, and the overall oxidation rates increased with increasing reduction temperature. From 1400 °C to 1500 °C, however, the loss in surface area was so significant that oxidation rates decreased, reflected by the large change in slope of the curve at 1500 °C. Thus, for WT ceria, operating with a reduction temperature of 1400 °C offered the best balance of the benefit of improved reduction thermodynamics (achieving $\delta \cong 0.01$ for the cycling conditions used in this study) with the loss of surface area due to sintering (SSA = 0.10 m^2 g^{-1}).

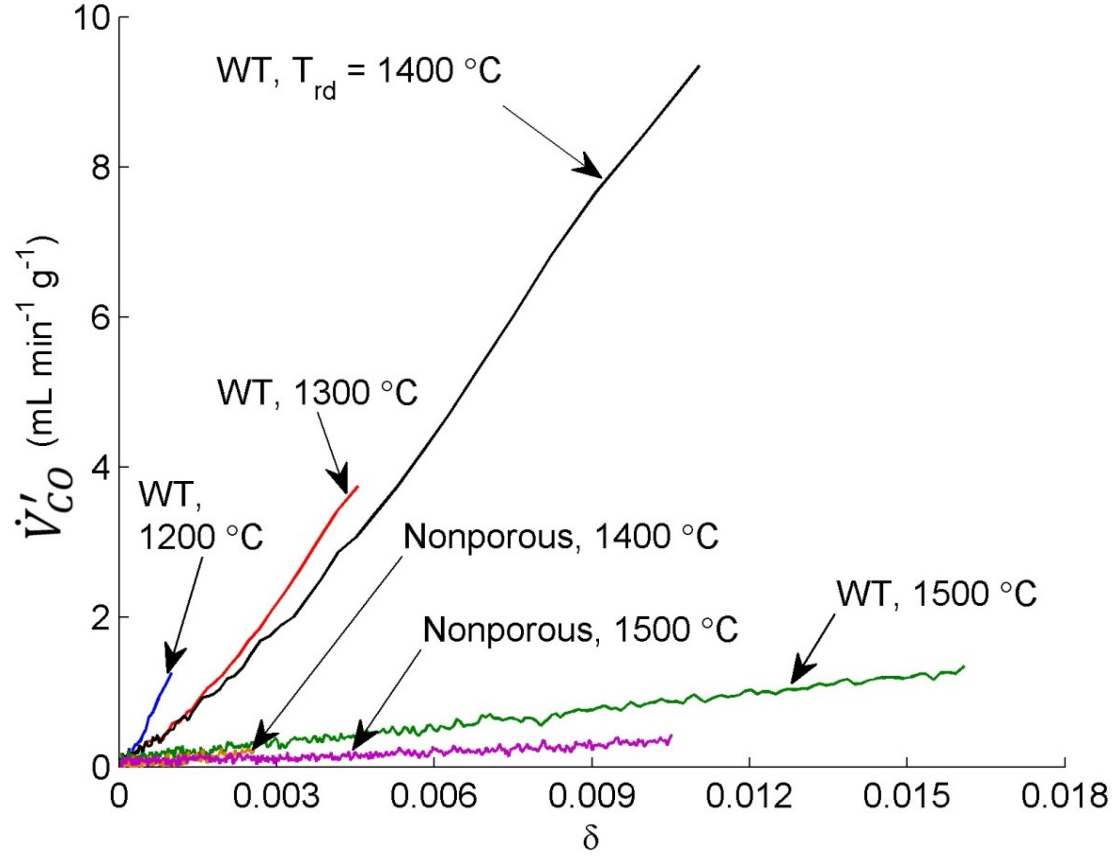

Figure 5.8 CO production rate as a function of δ for WT ceria at 800 °C following reduction at temperatures ranging from 1200–1500 °C and for nonporous ceria at 800 °C following reduction at 1400–1500 °C.

5.5 Summary and Conclusions

Wood templated ceria, a morphology that has not previously been studied for high temperature ceria-based fuel production, was thermochemically cycled in a laboratory-scale IR furnace. Ceria samples of 0.5 g were tested with an oxidation temperature of 800 °C and with reduction temperatures ranging from 1200–1500 °C. Sweep gas and CO_2 flows of 250 mL min^{-1} were introduced for reduction and oxidation, respectively. As the reduction temperature was increased, a tradeoff was found between the benefit of improved ceria thermodynamics and the drawback of surface area loss due to sintering. For WT ceria, increasing the reduction temperature from 1200–1400 °C led to an increase in the overall rate of CO production, but from 1400–1500 °C, the WT ceria sintered to such an extent that the overall oxidation rates decreased.

Oxidation rates were compared on the basis of ceria non-stoichiometry. This method allowed the effect of ceria non-stoichiometry on the rates of oxidation to be distinguished from the effect of the morphology, which is useful for studying the performance of a ceria morphology after sintering at different temperatures and for comparing oxidation rate data which began at different non-stoichiometries.

WT ceria was compared with a nonporous ceria powder. The WT ceria performed much better than the nonporous ceria: at a reduction temperature of 1400 °C, the WT ceria produced CO 5–6 times faster than the nonporous powder, when compared at the same δ. Even after the WT ceria sintered substantially at 1500 °C, it produced CO 2–3 times faster than the nonporous powder.

WT ceria is a promising candidate for efficient production of CO via solar-driven thermochemical cycling. This study showed that a reduction temperature of 1500 °C is not recommended for WT ceria due to considerable sintering of the WT ceria morphology. However, at a reduction temperature of 1400 °C, WT ceria retained a SSA of 0.1 m^2 g^{-1} and produced CO at peak rates of 9 mL min^{-1} g^{-1} for the cycling conditions used in this study.

6 Summary and Conclusions

Two approaches to improving the efficiency of solar-driven ceria redox cycling were examined. First, the gas flow rates and reduction and oxidation periods of an isothermal CO_2 splitting cycle were optimized to improve the cycle efficiency. In connection with this work, a quasi-equilibrium model of ceria reduction and oxidation was developed and validated with experimental data. Second, wood templated ceria, a new morphology for ceria redox cycling, was tested as a means of improving cycle performance.

6.1 Optimization of Cycling Conditions

Solar-driven non-stoichiometric reduction and oxidation of ceria provides a renewable pathway for producing fuels. While the ceria cycle has been demonstrated on both laboratory and prototype reactor scales, little work has been put into optimizing the cycle operating conditions: flow rates of sweep gas and oxidizer, and periods of reduction and oxidation.

Isothermal CO production at 1500 °C in a packed bed of porous ceria pellets was demonstrated over a range of both sweep gas and oxidizer flow rates (50–600 mL min^{-1} g^{-1}). Both reduction and oxidation reactions were limited by mass transport at flow rates below 300 mL min^{-1} g^{-1} and were limited by the surface reactions at higher flow rates. The data were interpreted to find the average rate of fuel production for shorter cycles operating within the range of non-stoichiometries covered in the experiment. An energy balance on a solar reactor was used to predict process efficiency for thousands of potential cycling periods for every combination of the tested sweep gas and CO_2 flow rates, assuming a concentration ratio of 3000 and 90% heat recovery effectiveness for both gas flows. The cycling conditions which led to the highest process efficiency for isothermal CO production at 1500 °C are a sweep gas flow rate of 150 mL min^{-1} g^{-1}, a CO_2 flow rate of 50 mL min^{-1} g^{-1}, a reduction period of 100 s, and an oxidation period of 155 s. Over 102 cycles, these optimal conditions yielded an average fuel production rate of 0.079 μmol s^{-1} g^{-1}. Assuming a concentration ratio of 3000, 90% gas phase heat recovery effectiveness, and that convective losses are 20% of the absorbed solar energy, the predicted reactor efficiency is 4.0%.

An analysis of the dimensionless scaling parameters originating from the volume-averaged conservation of species equation showed that matching the Damköhler number is required to scale up benchtop results to the scale of a solar reactor. If the morphology of the ceria is kept the same at both scales, matching the Damköhler number is accomplished by increasing the gas flow rates in proportion to the ceria mass.

There is further work to be done in optimizing the cycling conditions of the ceria cycle to improve process efficiency. One possible avenue for improvement would be to use a small temperature swing—smaller than the ~600–700 °C typically used in temperature-swing operation—that could combine the advantages of temperature-swing operation (better thermodynamics, lower reradiation losses during oxidation, lower sensible heating requirement of oxidizer) and isothermal operation (avoids requirement of solid-phase heat recovery, lower cyclic thermal stresses). Introducing a temperature swing would likely require a reassessment of the optimal gas flow rates and cycling periods; the general procedure used in Chapter 3 could be modified to account for a temperature swing. Another potential improvement worth exploring would be to operate reduction at a subatmospheric pressure in order to lower or eliminate the sweep gas requirement, which is a major energy sink in the cycle.

6.2 Quasi-equilibrium Model of Reaction Rates

Motivated by the observed mass transport limitation of isothermal reduction and oxidation rates at gas flow rates below 300 mL min^{-1} g^{-1}, a quasi-equilibrium model was developed to predict the rates of O_2 and CO production. The model was in close agreement with experimental results for sweep gas flows of 300 mL min^{-1} g^{-1} or less and CO_2 flows of 150 mL min^{-1} g^{-1} or less. The model also showed agreement with reduction data during a temperature swing with a ramp rate of 100 °C min^{-1}. The quasi-equilibrium model was used to show how long it would take to reach equilibrium in sweep gas of low O_2 concentration.

The quasi-equilibrium model could be applied to a discretized domain to capture the effects of gradients in δ. This has previously been done for reduction [33], but could be extended to include oxidation (over the appropriate range of flow rates).

6.3 Testing of Ceria Morphologies

Another way to increase the efficiency of the ceria cycle (in particular, the temperature-swing ceria cycle) is to improve the ceria morphology. The high temperatures required for ceria reduction tend to sinter morphologies which have the high surface areas beneficial to the surface-limited oxidation of temperature-swing cycling. Wood templated ceria, a morphology not previously used for high temperature redox cycling, was tested at reduction temperatures of 1200–1500 °C to investigate its cycle performance and resistance to sintering. Oxidation rate data was plotted as a function of ceria non-stoichiometry and used to analyze the oxidation performance of WT ceria after reduction at different temperatures and to compare its performance with that of a nonporous ceria powder. The wood templated ceria performed well at a reduction temperature of 1400 °C (peak CO production rates were 9 mL min^{-1} g^{-1}), but sintered significantly at a reduction temperature of 1500 °C (peak CO production rates were less than 2 mL min^{-1} g^{-1}). At both 1400 °C and 1500 °C, the performance of WT ceria was superior to that of the nonporous ceria powder.

Future work with ceria morphologies could explore different wood templates for ceria. In this study, a single type of wood (*P. strobus*) was examined. However, different species of trees have different wood microstructures, so it may be possible to select a different wood template which provides superior surface area and/or sintering resistance.

References

[1] Lovegrove, K., and Luzzi, A., 2003, "Solar Thermal Power Systems," Encyclopedia of Physical Science & Technology (Third Edition), R.A. Meyers, ed., Academic Press, New York, pp. 223–235.

[2] Venstrom, L. J., De Smith, R. M., Hao, Y., Haile, S. M., and Davidson, J. H., 2014, "Efficient Splitting of CO_2 in an Isothermal Redox Cycle Based on Ceria," Energy & Fuels, **28**(4), pp. 2732–2742.

[3] Steinfeld, A., 2005, "Solar Thermochemical Production of Hydrogen—a Review," Sol. Energy, **78**(5), pp. 603–615.

[4] Nakamura, T., 1977, "Hydrogen Production from Water Utilizing Solar Heat at High Temperatures," Sol. Energy, **19**(5), pp. 467–475.

[5] Kogan, A., 1998, "Direct Solar Thermal Splitting of Water and On-site Separation of the Products-II. Experimental Feasibility Study," Int. J. Hydrogen Energy, **23**(2), pp. 89–98.

[6] Kodama, T., and Gokon, N., 2007, "Thermochemical Cycles for High-temperature Solar Hydrogen Production," Chem. Rev., **107**(10), pp. 4048–77.

[7] Kodama, T., Kondoh, Y., Yamamoto, R., Andou, H., and Satou, N., 2005, "Thermochemical Hydrogen Production by a Redox System of ZrO_2-supported Co(II)-ferrite," Sol. Energy, **78**(5), pp. 623–631.

[8] Kodama, T., Gokon, N., and Yamamoto, R., 2008, "Thermochemical Two-step Water Splitting by ZrO_2-supported $Ni_xFe_{3-x}O_4$ for Solar Hydrogen Production," Sol. Energy, **82**(1), pp. 73–79.

[9] Panlener, R. J., Blumenthal, R. N., and Garnier, J. E., 1975, "A Thermodynamic Study of Nonstoichiometric Cerium Dioxide," J. Phys. Chem. Solids, **36**(11), pp. 1213–1222.

[10] Chueh, W. C., and Haile, S. M., 2010, "A Thermochemical Study of Ceria: Exploiting an Old Material for New Modes of Energy Conversion and CO_2 Mitigation.," Philos. Trans. R. Soc. A, **368**(1923), pp. 3269–94.

[11] Rudisill, S. G., Venstrom, L. J., Petkovich, N. D., Quan, T., Hein, N., Boman, D. B., Davidson, J. H., and Stein, A., 2013, "Enhanced Oxidation Kinetics in Thermochemical Cycling of CeO_2 through Templated Porosity," J. Phys. Chem. C, **117**(4), pp. 1692–1700.

[12] Gibbons, W. T., Venstrom, L. J., De Smith, R. M., Davidson, J. H., and Jackson, G. S., 2014, "Ceria-based Electrospun Fibers for Renewable Fuel Production via Two-Step Thermal Redox Cycles for Carbon Dioxide Splitting," Phys. Chem. Chem. Phys., Accepted.

[13] Venstrom, L. J., Petkovich, N. D., Rudisill, S. G., Stein, A., and Davidson, J. H., 2012, "The Effects of Morphology on the Oxidation of Ceria by Water and Carbon Dioxide," J. Sol. Energy Eng., **134**(1), p. 011005.

[14] Petkovich, N. D., Rudisill, S. G., Venstrom, L. J., Boman, D. B., Davidson, J. H., and Stein, A., 2011, "Control of Heterogeneity in Nanostructured $Ce_{1-x}Zr_xO_2$ Binary Oxides for Enhanced Thermal Stability and Water Splitting Activity," J. Phys. Chem. C, **115**(43), pp. 21022–21033.

[15] Chueh, W. C., Falter, C., Abbott, M., Scipio, D., Furler, P., Haile, S. M., and Steinfeld, A., 2010, "High-flux Solar-driven Thermochemical Dissociation of CO_2 and H_2O using Nonstoichiometric Ceria.," Science, **330**(6012), pp. 1797–801.

[16] Furler, P., Scheffe, J. R., and Steinfeld, A., 2012, "Syngas Production by Simultaneous Splitting of H_2O and CO_2 via Ceria Redox Reactions in a High-temperature Solar Reactor," Energy Environ. Sci., **5**(3), p. 6098.

[17] Furler, P., Scheffe, J. R., Gorbar, M., Moes, L., Vogt, U., and Steinfeld, A., 2012, "Solar Thermochemical CO_2 Splitting Utilizing a Reticulated Porous Ceria Redox System," Energy & Fuels, **26**, pp. 7051–7059.

[18] Lapp, J., Davidson, J. H., and Lipiński, W., 2012, "Efficiency of Two-step Solar Thermochemical Non-stoichiometric Redox Cycles with Heat Recovery," Energy, **37**(1), pp. 591–600.

[19] Ermanoski, I., Siegel, N. P., and Stechel, E. B., 2013, "A New Reactor Concept for Efficient Solar-Thermochemical Fuel Production," J. Sol. Energy Eng., **135**(3), p. 031002.

[20] Bader, R., Venstrom, L. J., Davidson, J. H., and Lipiński, W., 2013, "Thermodynamic Analysis of Isothermal Redox Cycling of Ceria for Solar Fuel Production," Energy & Fuels, **27**(9), pp. 5533–5544.

[21] Hao, Y., Yang, C.-K., and Haile, S. M., 2013, "High-temperature Isothermal Chemical Cycling for Solar-driven Fuel Production," Phys. Chem. Chem. Phys., **15**(40), pp. 17084–92.

[22] Diver, R. B., Miller, J. E., Allendorf, M. D., Siegel, N. P., and Hogan, R. E., 2008, "Solar Thermochemical Water-Splitting Ferrite-Cycle Heat Engines," J. Sol. Energy Eng., **130**(4), p. 041001.

[23] Lapp, J., Davidson, J. H., and Lipiński, W., 2013, "Heat Transfer Analysis of a Solid-Solid Heat Recuperation System for Solar-Driven Nonstoichiometric Redox Cycles," J. Sol. Energy Eng., **135**(3), p. 031004.

[24] Muhich, C. L., Evanko, B. W., Weston, K. C., Lichty, P., Liang, X., Martinek, J., Musgrave, C. B., and Weimer, A. W., 2013, "Efficient Generation of H_2 by Splitting Water with an Isothermal Redox Cycle.," Science, **341**(6145), pp. 540–2.

[25] Scheffe, J. R., and Steinfeld, A., 2012, "Thermodynamic Analysis of Cerium-Based Oxides for Solar Thermochemical Fuel Production," Energy & Fuels, **26**(3), pp. 1928–1936.

[26] Siegel, N. P., Miller, J. E., Ermanoski, I., Diver, R. B., and Stechel, E. B., 2013, "Factors Affecting the Efficiency of Solar Driven Metal Oxide Thermochemical Cycles," Ind. Eng. Chem. Res., **52**(9), pp. 3276–3286.

[27] Furler, P., Scheffe, J., Marxer, D., Gorbar, M., Bonk, A., Vogt, U. F., and Steinfeld, A., 2014, "Thermochemical CO_2 Splitting via Redox Cycling of Ceria Reticulated Foam Structures with Dual-Scale Porosities," Phys. Chem. Chem. Phys.

[28] Bader, R., Bala Chandran, R., Sedler, S. J., De Smith, R. M., Venstrom, L. J., Banerjee, A., Krenzke, P. T., Chase, T. R., Davidson, J. H., and Lipiński, W., "Design of a Solar Reactor for Splitting CO_2 Using Isothermal Redox Cycling of Ceria," Unpublished.

[29] Levenspiel, O., 1999, Chemical Reaction Engineering, Wiley, New York.

[30] Weisz, P. B., and Hicks, J. S., 1962, "The Behaviour of Porous Catalyst Particles in View of Internal Mass and Heat Diffusion Effects," Chem. Eng. Sci., **17**(4), pp. 265–275.

[31] Meier, A., Bonaldi, E., Cella, G. M., Lipiński, W., and Wuillemin, D., 2006, "Solar Chemical Reactor Technology for Industrial Production of Lime," Sol. Energy, **80**(10), pp. 1355–1362.

[32] Bulfin, B., Lowe, A. J., Keogh, K. A., Murphy, B. E., Lübben, O., Krasnikov, S. A., and Shvets, I. V., 2013, "Analytical Model of CeO_2 Oxidation and Reduction," J. Phys. Chem. C, **117**(46), pp. 24129–24137.

[33] Keene, D. J., Lipiński, W., and Davidson, J. H., 2014, "The Effects of Morphology on the Thermal Reduction of Nonstoichiometric Ceria," Chem. Eng. Sci., **111**, pp. 231–243.

[34] Zhao, C. Y., 2012, "Review on Thermal Transport in High Porosity Cellular Metal Foams with Open Cells," Int. J. Heat Mass Transf., **55**(13-14), pp. 3618–3632.

[35] Wu, Z., Caliot, C., Flamant, G., and Wang, Z., 2011, "Coupled Radiation and Flow Modeling in Ceramic Foam Volumetric Solar Air Receivers," Sol. Energy, **85**(9), pp. 2374–2385.

[36] Hischier, I., Leumann, P., and Steinfeld, A., 2012, "Experimental and Numerical Analyses of a Pressurized Air Receiver for Solar-Driven Gas Turbines," J. Sol. Energy Eng., **134**(2), p. 021003.

[37] Petrasch, J., Wyss, P., and Steinfeld, A., 2007, "Tomography-based Monte Carlo Determination of Radiative Properties of Reticulate Porous Ceramics," J. Quant. Spectrosc. Radiat. Transf., **105**(2), pp. 180–197.

[38] Malonzo, C. D., and Stein, A., 2014, University of Minnesota, Department of Chemistry, private communication.

[39] Keene, D. J., 2013, "Numerical Modeling of Transport Phenomena in Reactive Porous Structures for Solar Fuel Applications," Ph.D. thesis, Mechanical Engineering, University of Minnesota.

[40] Mills, A. F., 1999, Basic Heat and Mass Transfer, Prentice Hall, Upper Saddle River, New Jersey.

Appendix A: Scaling Parameters

To derive the dimensionless scaling parameters for the pellet bed, we start with the conservation of species equation (molar basis) [40],

$$\frac{\partial c_\mathrm{i}}{\partial t} + \nabla \cdot \left(c_\mathrm{i} \vec{u} - c_\mathrm{f} \mathcal{D}_\mathrm{i,eff} \nabla x_\mathrm{i} \right) = R_\mathrm{i}'''. \tag{A.1}$$

For porous media, all properties are evaluated as volume-averaged effective properties and the first term must include the porosity:

$$\frac{\partial c_\mathrm{i}}{\partial t} = \frac{\partial}{\partial t}(\phi c_\mathrm{i}). \tag{A.2}$$

In cylindrical coordinates (appropriate for tubular reactive elements):

$$\frac{\partial}{\partial t}(\phi c_\mathrm{i}) + \frac{1}{r}\frac{\partial}{\partial r}\left(\mathrm{r} c_\mathrm{i} u_\mathrm{r} - r c_\mathrm{f} \mathcal{D}_\mathrm{i,eff} \frac{\partial x_\mathrm{i}}{\partial r} \right) + \frac{\partial}{\partial z}\left(c_\mathrm{i} u_\mathrm{z} - c_\mathrm{f} \mathcal{D}_\mathrm{i,eff} \frac{\partial x_\mathrm{i}}{\partial z} \right) = R_\mathrm{i}'''. \tag{A.3}$$

Expressing the species concentration as the product of the overall fluid concentration and the species mole fraction,

$$c_\mathrm{i} = c_\mathrm{f} x_\mathrm{i}, \tag{A.4}$$

equation (A.3) is rewritten as

$$\begin{aligned} &\frac{\partial}{\partial t}(\phi c_\mathrm{f} x_\mathrm{i}) + \frac{\partial}{\partial z}(c_\mathrm{f} x_\mathrm{i} u_\mathrm{z}) + \frac{1}{r}\frac{\partial}{\partial r}(\mathrm{r} c_\mathrm{f} x_\mathrm{i} u_\mathrm{r}) \\ &\qquad = \frac{\partial}{\partial z}\left(c_\mathrm{f} \mathcal{D}_\mathrm{i,eff} \frac{\partial x_\mathrm{i}}{\partial z} \right) + \frac{1}{r}\frac{\partial}{\partial r}\left(\mathrm{r} c_\mathrm{f} \mathcal{D}_\mathrm{i,eff} \frac{\partial x_\mathrm{i}}{\partial r} \right) + R_\mathrm{i}'''. \end{aligned} \tag{A.5}$$

The following dimensionless scaling parameters are introduced:

$$z^* = \frac{z}{L},\ r^* = \frac{r}{R_\mathrm{bed}}, c_\mathrm{f}^* = \frac{c_\mathrm{f}}{c_\mathrm{f}^o}, u^* = \frac{u}{U}, \mathfrak{R} = \frac{R_\mathrm{i}'''}{\mathfrak{R}_\mathrm{ref}}, t^* = \frac{t}{\tau_\mathrm{res}} = \frac{tU}{L}, \tag{A.6}$$

where an asterisk denotes a dimensionless parameter and c_f^o and $\mathfrak{R}_\mathrm{ref}$ are evaluated at the inlet of the pellet bed. Using the dimensionless parameters in equation (A.6), equation (A.5) is expressed as

$$\begin{aligned}\frac{c_\mathrm{f}^o U}{L}\frac{\partial}{\partial t^*}(\phi c_\mathrm{f}^* x_\mathrm{i}) + \frac{c_\mathrm{f}^o U}{L}\frac{\partial}{\partial z^*}(c_\mathrm{f}^* x_\mathrm{i} u_\mathrm{z}^*) + \frac{c_\mathrm{f}^o U}{R_\mathrm{bed}}\frac{1}{r^*}\frac{\partial}{\partial r^*}(\mathrm{r}^* c_\mathrm{f}^* x_\mathrm{i} u_\mathrm{r}^*) \\ = \frac{c_\mathrm{f}^o \mathcal{D}_\mathrm{i,eff}}{L^2}\frac{\partial}{\partial z^*}\left(c_\mathrm{f}^*\frac{\partial x_\mathrm{i}}{\partial z^*}\right) + \frac{c_\mathrm{f}^o \mathcal{D}_\mathrm{i,eff}}{{R_\mathrm{bed}}^2}\frac{1}{r^*}\frac{\partial}{\partial r^*}\left(\mathrm{r}^* c_\mathrm{f}^*\frac{\partial x_\mathrm{i}}{\partial r^*}\right) \\ + \mathfrak{R}\mathfrak{R}_\mathrm{ref}.\end{aligned} \tag{A.7}$$

Multiplying by $\frac{L}{c_\mathrm{f}^o U}$ yields:

$$\begin{aligned}\frac{\partial}{\partial t^*}(\phi c_\mathrm{f}^* x_\mathrm{i}) + \frac{\partial}{\partial z^*}(c_\mathrm{f}^* x_\mathrm{i} u_\mathrm{z}^*) + \frac{L}{R_\mathrm{bed}}\frac{1}{r^*}\frac{\partial}{\partial r^*}(\mathrm{r}^* c_\mathrm{f}^* x_\mathrm{i} u_\mathrm{r}^*) \\ = \frac{\mathcal{D}_\mathrm{i,eff}}{UL}\frac{\partial}{\partial z^*}\left(c_\mathrm{f}^*\frac{\partial x_\mathrm{i}}{\partial z^*}\right) + \frac{L\mathcal{D}_\mathrm{i,eff}}{U{R_\mathrm{bed}}^2}\frac{1}{r^*}\frac{\partial}{\partial r^*}\left(\mathrm{r}^* c_\mathrm{f}^*\frac{\partial x_\mathrm{i}}{\partial r^*}\right) \\ + \frac{L\mathfrak{R}_\mathrm{ref}}{c_\mathrm{f}^o U}\mathfrak{R}.\end{aligned} \tag{A.8}$$

Expressing equation (A.8) in terms of the pellet bed aspect ratio,

$$\Gamma = \frac{L}{R_\mathrm{bed}}, \tag{A.9}$$

the Peclet number,

$$Pe_L = \frac{UL}{\mathcal{D}_\mathrm{i,eff}}, \tag{A.10}$$

and the Damköhler number,

$$Da = \frac{L/U}{c_\mathrm{f}^o/\mathfrak{R}_\mathrm{ref}} = \frac{L/U}{c_\mathrm{f}^o/\dot{n}_\mathrm{i,ref}'' a}, \tag{A.11}$$

yields:

$$\begin{aligned}\frac{\partial}{\partial t^*}(\phi c_{\mathrm{f}}^* x_{\mathrm{i}}) + \frac{\partial}{\partial z^*}(c_{\mathrm{f}}^* x_{\mathrm{i}} u_{\mathrm{z}}^*) + \Gamma \frac{1}{r^*}\frac{\partial}{\partial r^*}(\mathrm{r}^* c_{\mathrm{f}}^* x_{\mathrm{i}} u_{\mathrm{r}}^*) \\ = \frac{1}{Pe_L}\frac{\partial}{\partial z^*}\left(c_{\mathrm{f}}^* \frac{\partial x_{\mathrm{i}}}{\partial z^*}\right) + \frac{\Gamma^2}{Pe_L}\frac{1}{r^*}\frac{\partial}{\partial r^*}\left(\mathrm{r}^* c_{\mathrm{f}}^* \frac{\partial x_{\mathrm{i}}}{\partial r^*}\right) + Da\mathfrak{R}.\end{aligned} \tag{A.12}$$

Now, if radial gradients are negligible (thus making the problem one dimensional in the z-direction), equation (A.12) simplifies to:

$$\frac{\partial}{\partial t^*}(\phi c_{\mathrm{f}}^* x_{\mathrm{i}}) + \frac{\partial}{\partial z^*}(c_{\mathrm{f}}^* x_{\mathrm{i}} u_{\mathrm{z}}^*) = \frac{1}{Pe_L}\frac{\partial}{\partial z^*}\left(c_{\mathrm{f}}^* \frac{\partial x_{\mathrm{i}}}{\partial z^*}\right) + Da\mathfrak{R}, \tag{A.13}$$

where it should be noted that the pellet bed aspect ratio (Γ) no longer appears. If the Peclet number is large ($Pe_{\mathrm{L}} \gg 1$), equation (A.13) can be further simplified to:

$$\frac{\partial}{\partial t^*}(\phi c_{\mathrm{f}}^* x_{\mathrm{i}}) + \frac{\partial}{\partial z^*}(c_{\mathrm{f}}^* x_{\mathrm{i}} u_{\mathrm{z}}^*) = Da\mathfrak{R}. \tag{A.14}$$

Significantly, under the assumptions of radial uniformity and a large Peclet number, the only dimensionless parameter that must be matched to ensure similarity of the conservation of species equation is the Damköhler number.

Appendix B: Cycling Data

This appendix contains the thermochemical cycling data in an IR imaging furnace discussed in Chapter 5. The data consist of 21 cycles each for wood templated ceria tested at reduction temperatures of 1200, 1300, 1400, and 1500 °C and for nonporous ceria tested at reduction temperatures of 1400 °C and 1500 °C. All oxidation temperatures were 800 °C, and temperature ramping rates were 200 °C min^{-1}. Sweep gas and CO_2 flows were 250 mL min^{-1}, and all ceria samples were 0.3 g.

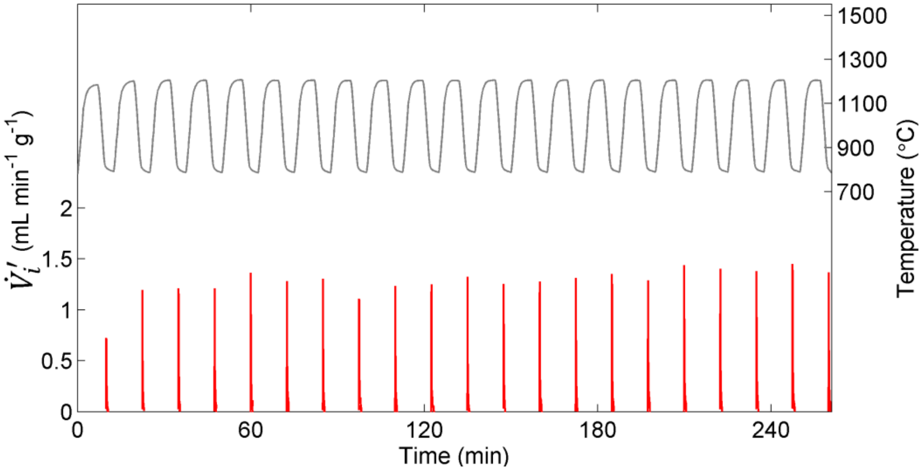

Figure B.1 Cycling data for WT ceria at a reduction temperature of 1200 °C. CO production rate (red) and temperature measurement from the thermocouple embedded in the ceria sample (gray) are shown over 21 cycles. O_2 production rates were below the detection limit of the RLGA.

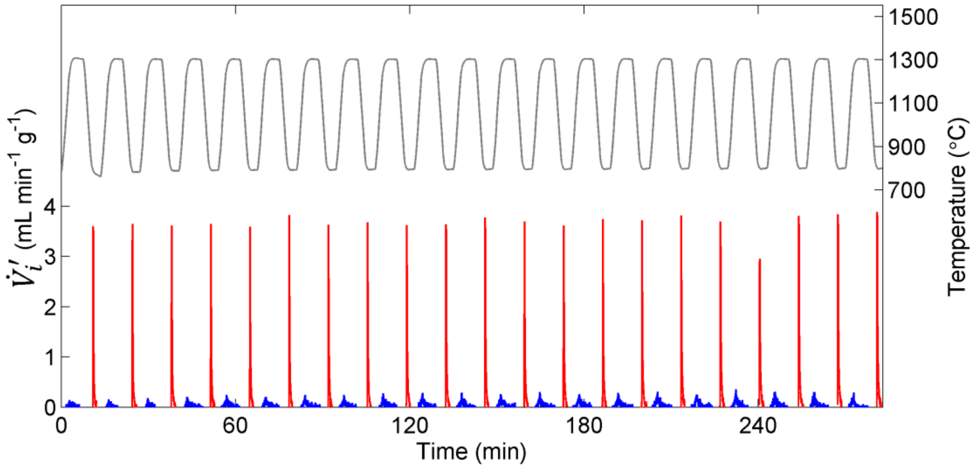

Figure B.2 Cycling data for WT ceria at a reduction temperature of 1300 °C. CO (red) and O_2 (blue) production rates and the temperature measurement from the thermocouple embedded in the ceria sample (gray) are shown over 21 cycles.

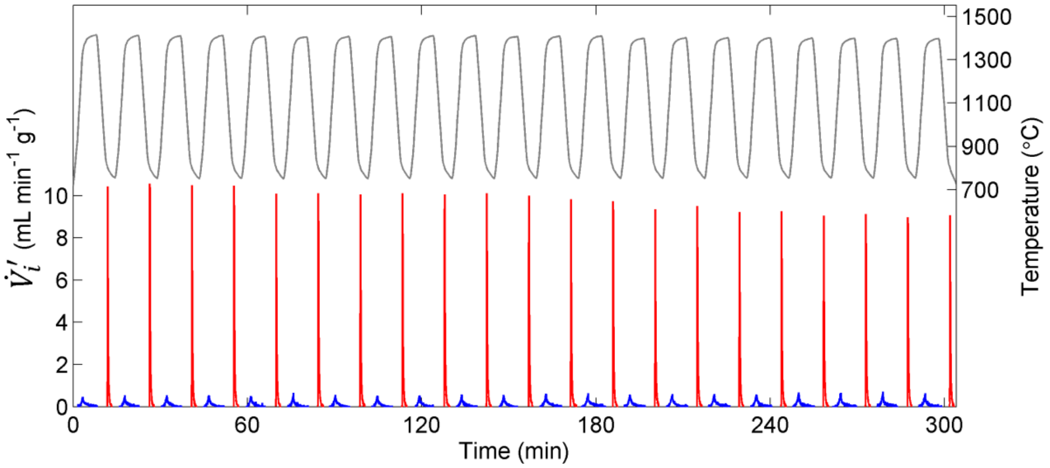

Figure B.3 Cycling data for WT ceria at a reduction temperature of 1400 °C. CO (red) and O_2 (blue) production rates and the temperature measurement from the thermocouple embedded in the ceria sample (gray) are shown over 21 cycles.

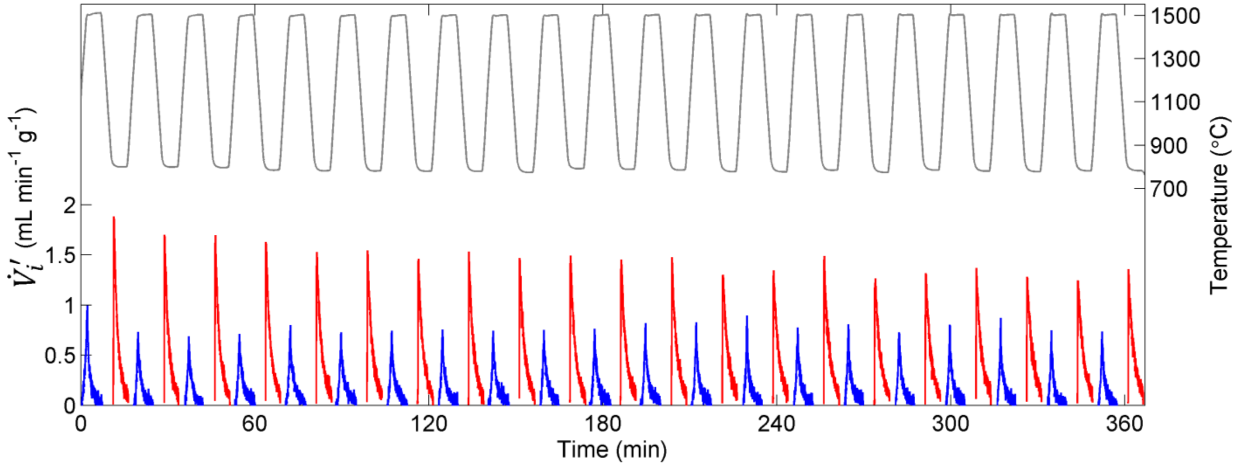

Figure B.4 Cycling data for WT ceria at a reduction temperature of 1500 °C. CO (red) and O_2 (blue) production rates and the temperature measurement from the thermocouple embedded in the ceria sample (gray) are shown over 21 cycles.

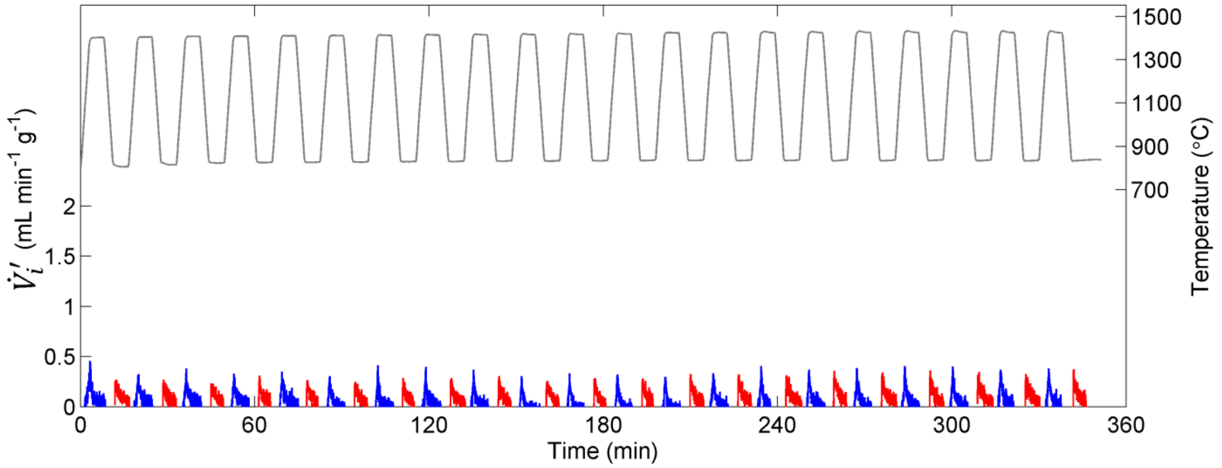

Figure B.5 Cycling data for nonporous ceria powder at a reduction temperature of 1400 °C. CO (red) and O_2 (blue) production rates and the temperature measurement from the thermocouple embedded in the ceria sample (gray) are shown over 21 cycles.

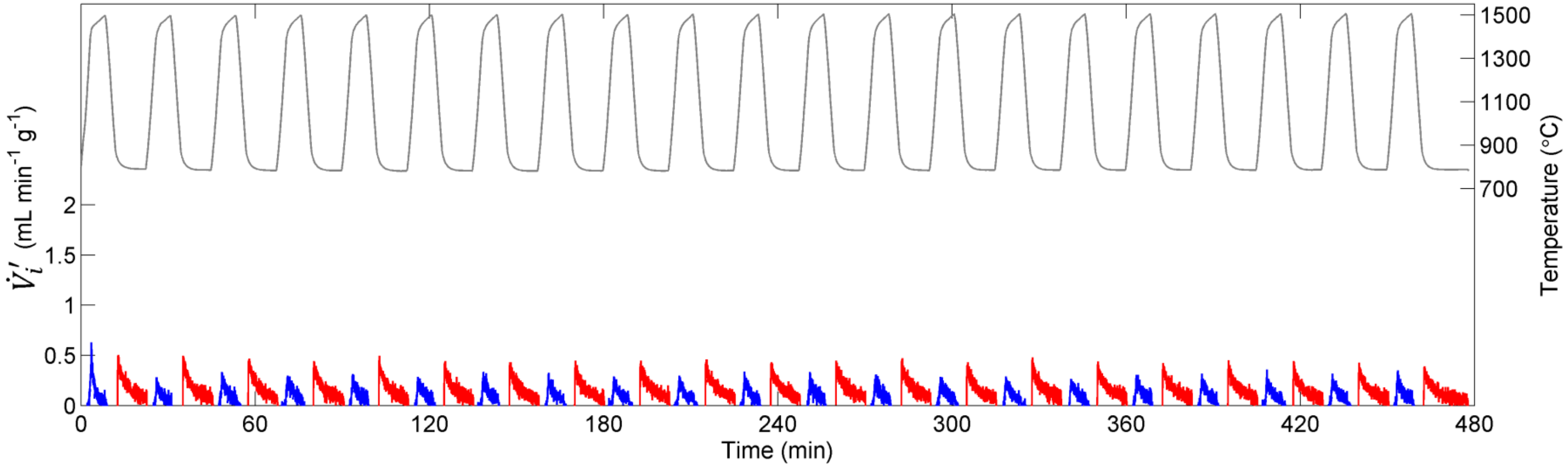

Figure B.6 Cycling data for nonporous ceria powder at a reduction temperature of 1500 °C. CO (red) and O_2 (blue) production rates and the temperature measurement from the thermocouple embedded in the ceria sample (gray) are shown over 21 cycles.